AGU PUBLICATIONS

JGR

Journal of Geophysical Research: Oceans

RESEARCH ARTICLE

10.1002/2015JC011153

Influence of varying upper ocean stratification on coastal near-inertial currents

Sung Yong Kim[1], Alexander L. Kurapov[2], and P. Michael Kosro[2]

[1]Department of Mechanical Engineering, School of Mechanical and Aerospace Engineering, Korea Advanced Institute of Science and Technology, Daejeon, Republic of Korea, [2]College of Earth, Ocean, and Atmospheric Sciences, Oregon State University, Corvallis, Oregon, USA

Key Points:
- Directly wind-forced near-inertial motions are enhanced under stratified conditions
- Reduced near-inertial motions and their offshore propagating phases indicate coastal inhibition
- Seasonal stratification and freshwater plumes lead to enhanced coastal near-inertial motions

Correspondence to:
S. Y. Kim,
syongkim@kaist.ac.kr

Citation:
Kim, S. Y., A. L. Kurapov, and P. Michael Kosro (2015), Influence of varying upper ocean stratification on coastal near-inertial currents, *J. Geophys. Res. Oceans*, *120*, 8504–8527, doi:10.1002/2015JC011153.

Received 20 JUL 2015
Accepted 13 NOV 2015
Accepted article online 18 NOV 2015
Published online 31 DEC 2015

Abstract The influence of varying horizontal and vertical stratification in the upper layer ($O(10)$ m) associated with riverine waters and seasonal atmospheric fluxes on coastal near-inertial currents is investigated with remotely sensed and in situ observations of surface and subsurface currents and realistic numerical model outputs off the coast of Oregon. Based on numerical simulations with and without the Columbia River (CR) during summer, the directly wind-forced near-inertial surface currents are enhanced by 30%–60% when the near-surface layer has a stratified condition due to riverine water inputs from the CR. Comparing model results without the CR for summer and winter conditions indicates that the directly wind-forced near-inertial surface current response to a unit wind forcing during summer are 20%–70% stronger than those during winter depending on the cross-shore location, which is in contrast to the seasonal patterns of both mixed-layer depth and amplitudes of near-inertial currents. The model simulations are used to examine aspects of coastal inhibition of near-inertial currents, manifested in their spatial coherence in the cross-shore direction, where the phase propagates upward over the continental shelf, bounces at the coast, and continues increasing upward offshore (toward surface) and then downward offshore at the surface, with magnitudes and length scales in the near-surface layer increasing offshore. This pattern exhibits a particularly well-organized structure during winter. Similarly, the raypaths of clockwise near-inertial internal waves are consistent with the phase propagation of coherence, showing the influence of upper layer stratification and coastal inhibition.

1. Introduction

Near-inertial motions in the ocean are mainly caused by wind stress variations on the time scale of a day or two [e.g., *Pollard and Millard*, 1970; *D'Asaro*, 1985]. The wind energy that penetrates the air-sea interface generates near-inertial oscillations, which are transformed by mixing and dissipation in the mixed layer and propagate into the ocean interior [e.g., *Gregg and Briscoe*, 1979; *Alford and Gregg*, 2001]. The near-inertial currents are significantly modified by the presence of the coast (and reduced in magnitude) within one or two internal radii of deformation from the coast [e.g., *Pettigrew*, 1981; *Kim et al*., 2011; *Shearman*, 2005].

The generation and propagation of coastal near-inertial waves have been addressed with a classical two-layer model [e.g., *Krauss*, 1972; *Flagg*, 1977; *Crepon*, 1969], demonstrating that stratification is a primary factor controlling the near-inertial currents in shelf areas and enclosed basins. In coastal areas, the reduction in the near-inertial amplitudes may result from frictional decay due to bottom friction, proximity of the shoreline (implying no-flow conditions), or the disappearance of stratification [e.g., *Pettigrew*, 1981]. *Crepon* [1969] studied transient ocean responses to a suddenly imposed constant wind stress and reported that inertial motions are generated at the coast and propagate seaward. *Pettigrew* [1981] reported that there is a 180° phase difference in near-inertial currents between surface and subsurface layers over the shelf and the locally generated near-inertial energy radiates seaward away from the coast.

Freshwater plumes discharged from coastal rivers drive a strong vertical density gradient in the upper layer and may generate surface-intensified wind responses [e.g., *Kim et al*., 2009a], eddies and bulge circulation [e.g., *O'Donnell*, 1990; *Berdeal et al*., 2002; *Kourafalou et al*., 1996], tidal modulation [e.g., *Verspecht et al*., 2010], and responses coupled with wind-driven upwelling and downwelling [e.g., *Choi and Wilkin*, 2007; *Kim et al*., 2009b; *Gan et al*., 2009; *Banas et al*., 2009; *Shrira and Forget*, 2015]. Seasonal variability in heat and

freshwater fluxes and wind stress leads to the changes in the depth of the surface mixed layer and stratification strength, causing modulation in the penetration depth of the wind stress momentum [e.g., *Shearman*, 2005]. For example, a well-stratified water column with a shallow pycnocline has a strong wind response confined near the surface, which would correspond to summer conditions in many regions including the U.S. West Coast (USWC). The near-inertial current response to winds in a deep mixed layer with higher eddy viscosity, corresponding to winter conditions along the USWC, is weaker at the surface and penetrates more deeply [e.g., *Price et al*., 1986; *Shearman*, 2005; *Kim et al*., 2009a]. Thus, modulations by freshwater inputs, heat fluxes, and wind-induced mixing generate variability in vertical energy propagation of coastal near-inertial motions on a seasonal time scale.

In the open ocean, downward propagation of near-inertial energy has been observed to be more dominant than upward propagation, as indicated by asymmetric vertical wave number spectra [e.g., *D'Asaro and Perkins*, 1984; *Large et al*., 1994; *Zervakis and Levine*, 1995; *Crawford and Large*, 1996]. Near-coastal boundaries, reflection from shoreline and bottom topography may be expected and the near-inertial oscillations exhibit "coastal inhibition," when the near-inertial energy propagates at an angle from the vertical, namely, downward and offshore from the surface-coast corner; at the same location the phase would propagate upward and offshore [e.g., *Kundu*, 1976; *Millot and Crepon*, 1981; *Pettigrew*, 1981; *Flagg*, 1977] (see *Kundu et al*. [1983], and *Kundu* [1984] for more observational details).

The two earlier companion papers [*Kim and Kosro*, 2013; *Kim et al*., 2014] to this work focused on near-inertial currents in the near-surface ocean (mainly the upper 1 m depth) in terms of decorrelation scales and wind transfer functions, with application to flows off Oregon (USWC). Specifically, *Kim and Kosro* [2013] estimated the decorrelation scales of near-inertial currents using high-frequency radar (HFR)-derived surface current data using spectral analysis and spatial coherence, which in particular provided a surface view of the coastal inhibition of near-inertial motions. *Kim et al*. [2014] studied directly wind-forced near-inertial surface currents with the isotropic wind transfer function analysis using only surface wind stress and surface currents obtained from numerical simulations and in situ observations. *Kim et al*. [2015] discussed the anisotropic wind transfer functions at three primary frequencies (low, diurnal, and inertial frequencies). In these studies, the near-inertial currents were estimated by averaging over a year, and the effects of seasonality in the atmospheric fluxes or the freshwater discharge were not considered. The influences of stratification and coastal inhibition have not been thoroughly considered. In this paper, we examine variability in near-inertial oscillations resulting from stratification changes due to freshwater inputs from the Columbia River (CR, in summer only) and seasonal atmospheric fluxes (summer versus winter) using moored observations of subsurface currents, temperature, and salinity and realistic numerical model outputs run with and without the CR. Our analysis also includes a study of the propagation and reflection of near-inertial energy at the coastal boundaries to examine "coastal inhibition," in particular, as this pattern exhibits seasonality.

This paper is organized as follows. Numerical simulation outputs and in situ observations are summarized with their spectral contents and time series in section 2. In section 3, the variance in the near-inertial currents and their wind-current transfer functions are compared along a cross-shore section for different stratification conditions. Particularly, the influences of riverine waters (section 3.2.2) and seasonal heat fluxes (section 3.2.3) on the clockwise near-inertial currents are discussed. In section 3.3, the coastal inhibition of clockwise near-inertial currents is examined with their spatial coherence along a cross-shore section. Summary and discussions of these analyses are presented in section 4.

2. Numerical Simulations and Observations

2.1. Study Domain

Numerical simulations using the Regional Ocean Modeling System (ROMS; www.myroms.org) have provided currents with an hourly temporal resolution and 2 km spatial resolution for a period of approximately 1 year (August 2008 to August 2009; see *Kim et al*. [2014] for more details). A subset of the domain (red boxes in Figures 1a and 1b) was chosen to overlap with an effective spatial coverage of HFR off the coast of Oregon, defined as the area with greater than 50% data availability over a period of 2 years (2008–2009) (a yellow contour in Figure 1b). The study domain is enclosed by a box ranging from 126.27°W to 123.82°W and from 42.81°N to 47.07°N, and the corresponding inertial frequencies (f_c) range from −1.359 cycles per day (cpd) to −1.464 cpd. Note that the clockwise near-inertial motions are dominant in the Northern

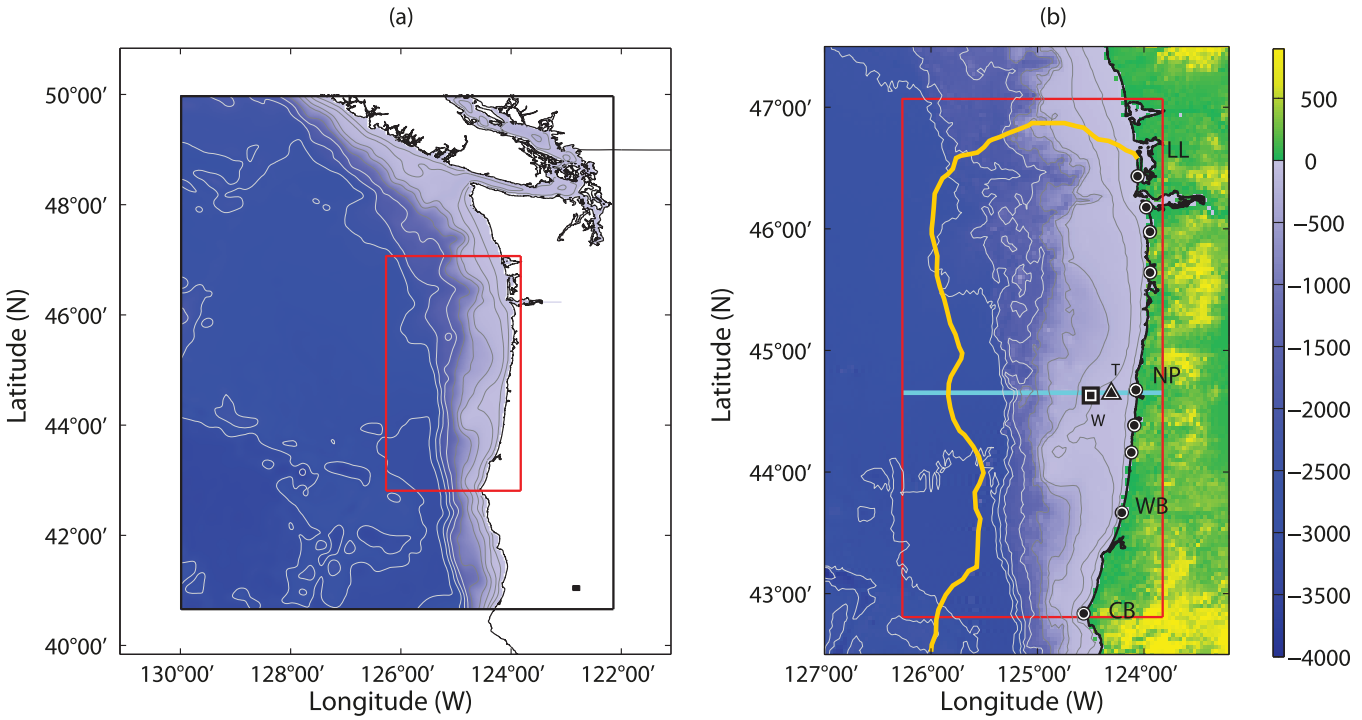

Figure 1. A study domain of the influence of freshwater from the CR on the near-inertial currents off the coast of Oregon. (a) The ROMS domain and its subset (a red rectangular box) and (b) in situ observations of the wind at the NDBC 46050 buoy (Stonewall bank; W; square), ADCP subsurface currents and CTD data at the NH10 mooring location (T; triangle), and surface currents from an array of HFRs (circles). A cross-shore line (cyan) closest to the NH10 mooring location represents the cross-shore structure of near-inertial currents. A yellow curve indicates the effective spatial coverage of the HFR surface current maps. The bottom bathymetry is contoured at 50, 100, 250, 500, 1000, 1500, 2000, 2500, and 3000 m. As a reference, major coastal regions are denoted by abbreviated two letter names from south to north: Cape Blanco (CB), Winchester Bay (WB), Newport (NP), and Loomis Lake (LL).

Hemisphere and by convention the clockwise inertial frequency is negative ($f_c < 0$). A cross-shore line at 44.647°N (NH line; a cyan line in Figure 1b; $f_c = -1.406$ cpd) is chosen to examine the cross-shore structure of near-inertial currents. The simulations were run unaided by data assimilation.

2.2. Numerical Simulations

The CR is discharged into the Pacific Ocean at Oregon's northern border (46.2°N). In winter, under downwelling winds, the CR plume waters most often turn to the north and do not affect stratification off Oregon. In spring-summer, as an effect of wind-driven upwelling, the CR plume is directed offshore and to the south of the river mouth [e.g., *Hickey et al.*, 2005, 2010], modifying near-surface stratification in an area, stretching for approximately 400 km in the alongshore and 200 km in the offshore direction. During periods of relaxation from upwelling to downwelling the plume waters are moved closer to the coast resulting in the freshening of the near-surface waters over the Oregon shelf.

Two model simulations, with and without the CR, were run for the period from August 2008 to August 2009. These are compared to examine the influence of the stratification change due to freshwater inputs in summer. The effect of seasonal change in horizontal and vertical stratification due to atmospheric fluxes is studied by comparing model results without the CR for the summer and winter periods. For convenience, in analyses below, a closed circle (•) and open circle (°) indicate the simulation outputs with and without the CR, respectively.

The model uses terrain-following vertical coordinates, and the model outputs have been obtained at 40 vertical levels. For present analyses, these are mapped to a *z*-grid with a spacing of 2 m from the surface to the bottom. The *u*-component and *v*-component of the model currents are not colocated as they are provided on sides of each computational cell on the staggered Arakawa "C" grid [*Arakawa*, 1966]. For analyses, they are linearly interpolated to the center of each grid cell.

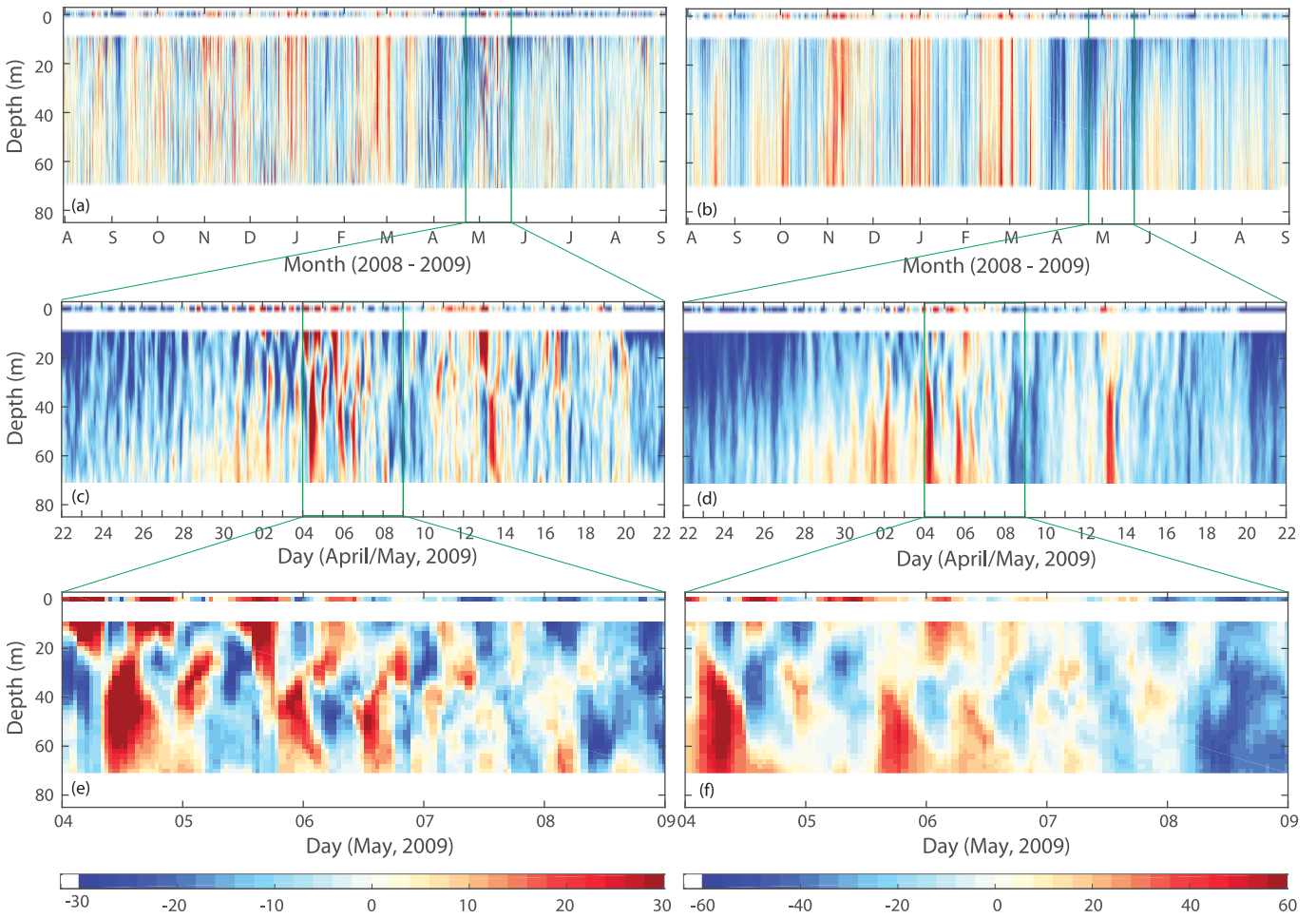

Figure 2. Time series of hourly averaged surface and subsurface currents at the NH10 mooring location (T in Figure 1b) for (a and b) a period of approximately 1 year (August 2008 to August 2009) and their two cascaded magnified views (c and d) for a period of 1 month (22 April 2009 to 21 May 2009) and (e and f) for a period of 5 days (4–8 May 2009). (a, c, and e) *u*-component (cm s^{-1}). (b, d, and f) *v*-component (cm s^{-1}). Green boxes in Figures 2a–2d denote the subsequent zoom-in plots in Figures 2c–2f, respectively.

2.3. Observations

2.3.1. Surface and Subsurface Currents

Hourly averaged surface currents are provided by a network of HFRs off the coast of Oregon [e.g., *Kosro*, 2005; *Kim and Kosro*, 2013]. Hourly averaged subsurface currents for the same time period (2008–2009) are obtained from a bottom-mounted upward-looking acoustic Doppler current profiler (ADCP), deployed at 80 m depth on the Newport (NH) line (T in Figure 1b) and located 10 nautical miles (18 km) from the coast (NH10 mooring) [e.g., *Kosro*, 2003]. The ADCP data are provided between depths of 10–68 m, in 2 m vertical bins.

The time series of current observations at the NH10 mooring location are presented with two time-depth sections of *u*-component and *v*-component (Figure 2) with close-ups in time that can highlight significant near-inertial motions at the surface and in the subsurface (see clockwise near-inertial amplitudes in Figures 5a–5c during early May of 2009). The yearlong current profiles exhibit the persistent poleward currents during winter (Figure 2b). The structures of vertically continuous currents and shear currents in the upper 5 m depth obtained from two independent observations (ADCP and HFR) are more visible at hourly time scale (Figures 2e and 2f).

Using concurrent surface and subsurface current data, we can examine the variance distribution of baroclinic and barotropic horizontal velocity components in the frequency domain by looking at the difference between the depth-averaged spectrum of subsurface currents ($\bar{S}_{\mathbf{u}}$) and the spectrum of depth-averaged subsurface currents ($S_{\bar{\mathbf{u}}}$) (Figures 3a and 3b). The depth-averaged spectrum ($\bar{S}_{\mathbf{u}}$) is computed as

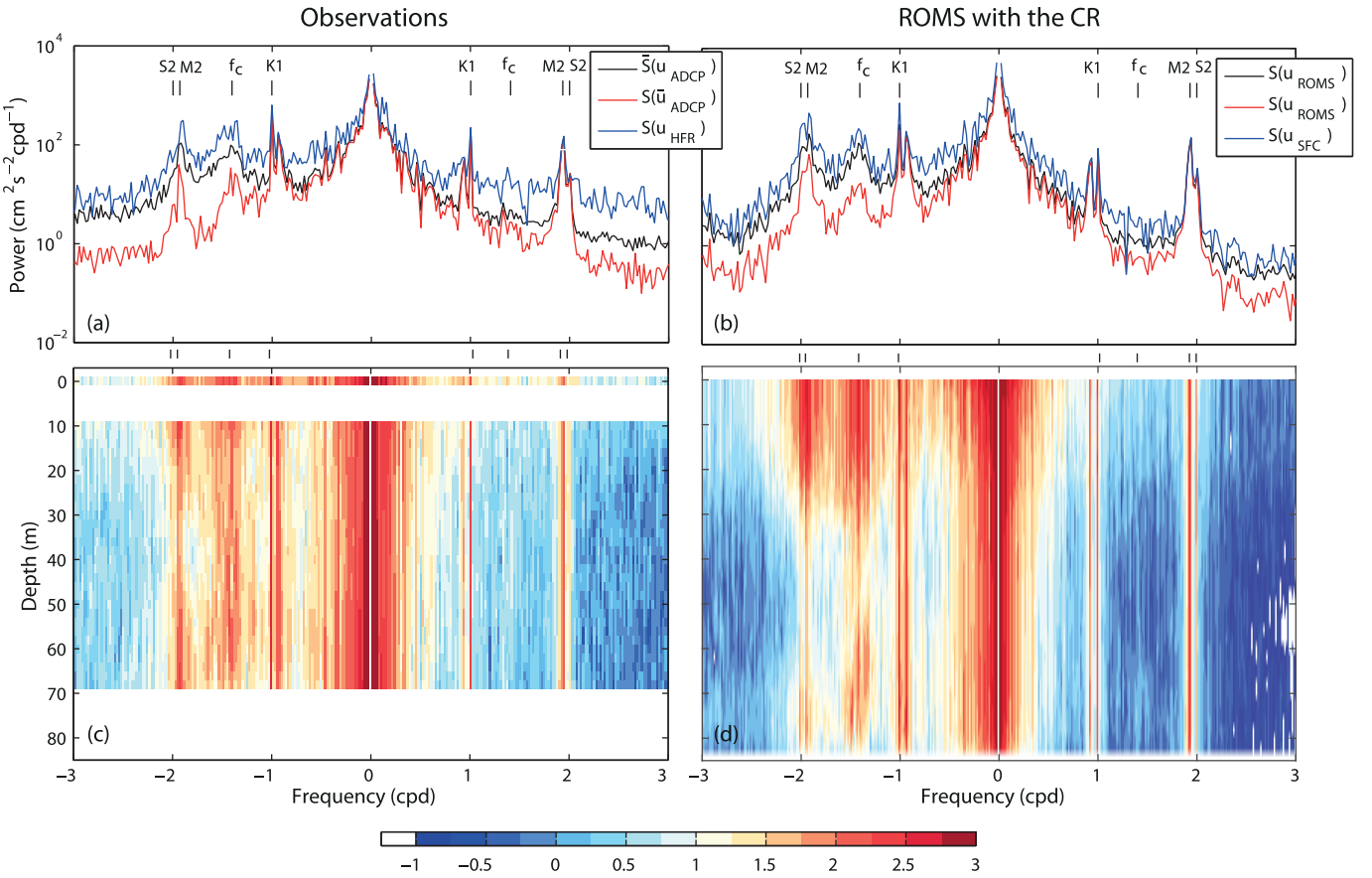

Figure 3. Rotary power spectra of surface and subsurface currents for a period of approximately 1 year (August 2008 to August 2009). Depth-averaged power spectrum of subsurface currents ($\bar{S}_{\mathbf{u}}$), power spectrum of depth-averaged subsurface currents ($S_{\bar{\mathbf{u}}}$), and power spectrum of surface (layer) currents ($S_{\mathbf{u}_{HFR}}$ or $S_{\mathbf{u}_{SFC}}$), based on (a) observations (HFR and ADCP) and (b) ROMS simulations with the CR (**u**.). Profiles of rotary power spectra ($\log_{10}$ scale, cm^2 s^{-2} cpd^{-1}) of surface and subsurface currents, based on (c) observations (HFR and ADCP) and (d) ROMS simulations with the CR (**u**.). The variance at the zero frequency, i.e., the mean in the time domain, is not shown in Figures 3a and 3b, because we can highlight variance at nonzero frequencies effectively. The primary frequencies (K_1, M_2, S_2, and f_c) appear as peaks in the spectrum and are marked on the top of each plot. Negative and positive frequencies correspond to clockwise and counter-clockwise rotations, respectively.

$$\bar{S}_{\mathbf{u}}(\sigma) = \frac{1}{h-a}\int_h^a S_{\mathbf{u}}(z,\sigma)\mathrm{d}z, \tag{1}$$

where $S_{\mathbf{u}}(z,\sigma)$ is the rotary spectrum of currents, $\mathbf{u}(z,t) = u(z,t) + iv(z,t)$, at individual depths ($z$), and integration limits (h and a) are from the bottom to surface (model) or the deepest and shallowest ADCP bins. Another spectrum ($S_{\bar{\mathbf{u}}}$) is computed for the depth-averaged currents:

$$\bar{\mathbf{u}}(t) = \frac{1}{h-a}\int_h^a \mathbf{u}(z,t)\mathrm{d}z. \tag{2}$$

Figure 3a shows that baroclinic currents (black line) are dominant over barotropic currents (red line) at clockwise M_2 frequency [e.g., *Kurapov et al.*, 2003] and in the near-inertial frequency band. The baroclinic and barotropic currents are nearly equivalent at the clockwise diurnal (K_1) frequency and counter-clockwise K_1 and M_2 frequencies, and in the low-frequency band in both rotations. The spectra of HFR-derived surface currents (blue line) and the depth-averaged spectrum of subsurface currents (black line) exhibit consistent spectral contents. In particular, near-inertial energy is enhanced for clockwise currents ($f_c < 0$).

Figure 3c shows the continuous vertical distribution of energy of the HFR-derived surface currents and ADCP-derived subsurface currents in the upper bins. The clockwise near-inertial variance is strong throughout the water column and is at its minimum between 30 and 40 m depth. The counter-clockwise variance in the near-inertial frequency band is negligible and is within the noise level. Additionally, the variance at low ($|\sigma| < 0.3$ cpd) and diurnal (both clockwise and counter-clockwise rotations) frequencies and counter-

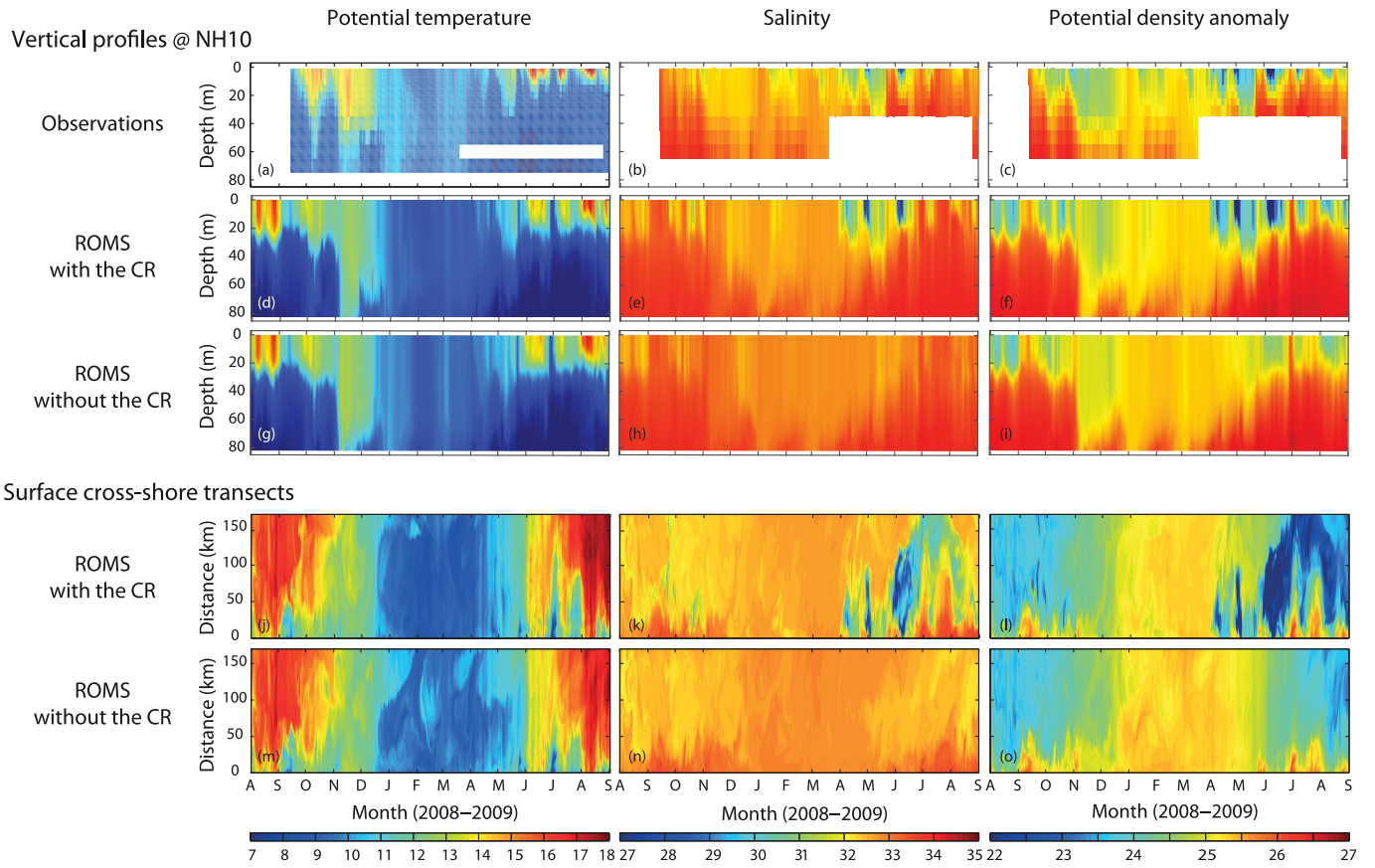

Figure 4. (a–i) Time series of daily averaged vertical profiles of potential temperature (°C), salinity, and potential density anomaly ($\rho' = \rho - 1000$; kg m^{-3}) as a function of depth, sampled at the NH10 mooring location. (a–c) Observations. The salinity sampled at 2, 10, 30, and 60 m is interpolated on the temperature sampling depths (2, 4, 6, 8, 10, 15, 20, 25, 30, 40, 50, 60, and 70 m). White areas indicate missing observations. (d–f) ROMS simulations with the CR ($T_.$, $S_.$, and $\rho'_.$). (g–i) ROMS simulations without the CR ($T_\circ$, $S_\circ$, and $\rho'_\circ$). (j–o) Time series of daily averaged surface potential temperature (°C), salinity, and potential density anomaly ($\rho' = \rho - 1000$; kg m^{-3}) as a function of cross-shore distance from the shore, obtained from ROMS simulations. (j–l) ROMS simulations with the CR ($T_.$, $S_.$, and $\rho'_.$). (m–o) ROMS simulations without the CR ($T_\circ$, $S_\circ$, and $\rho'_\circ$).

clockwise semidiurnal (M_2) frequencies become significant at most of the water depths (Figure 3c), corresponding to a predominantly barotropic signal [e.g., *Kurapov et al.*, 2003; *Osborne et al.*, 2011, 2014].

The energy spectra of hourly ROMS currents (**u.**), sampled at the same location as the ADCP, are presented in the same way (Figures 3b and 3d). The model-derived spectral contents and their distribution in depth are consistent with observations. The clockwise near-inertial energy is reduced between 40 and 60 m (Figure 3d).

2.3.2. Moored Temperature and Salinity Data

Vertical profiles of potential temperature were sampled every 2 min at the NH10 mooring location for a period of 19 months (September 2008 to April 2010), using 13 sensors (2, 4, 6, 8, 10, 15, 20, 25, 30, 40, 50, 60, and 70 m), and shown here for the period of model simulations (Figure 4a). Note that the temperature in the following sections is as potential temperature. Salinity time series were measured during the same period at four vertical levels (at 2, 10, 30, and 60 m) and linearly interpolated on the depths where temperature data were sampled (Figure 4b). For comparison, the ROMS simulations with and without the CR are presented as a time series of (1) vertical profiles of potential temperature, salinity, and potential density anomaly (Figures 4d–4i) at the NH10 mooring location and (2) cross-shore records of surface temperature ($T_.$ and $T_\circ$), salinity ($S_.$ and $S_\circ$), and density ($\rho_.$ and $\rho_\circ$) (Figures 4j–4o). In both cases, the temperature profiles in the vertical and cross-shore directions show similar seasonal variability, caused by seasonal heat fluxes and the strength of upwelling (Figures 4d, 4j, 4g, and 4m). The change in vertical stratification in the upper 30 m due to the CR becomes significant (Figures 4f and 4i). The low-salinity water in summer (June–August 2009) extends beyond 150 km offshore (Figure 4k) and 400 km to the south from the river mouth, reducing the surface water density by approximately 2 kg m^{-3} at the NH10 mooring location.

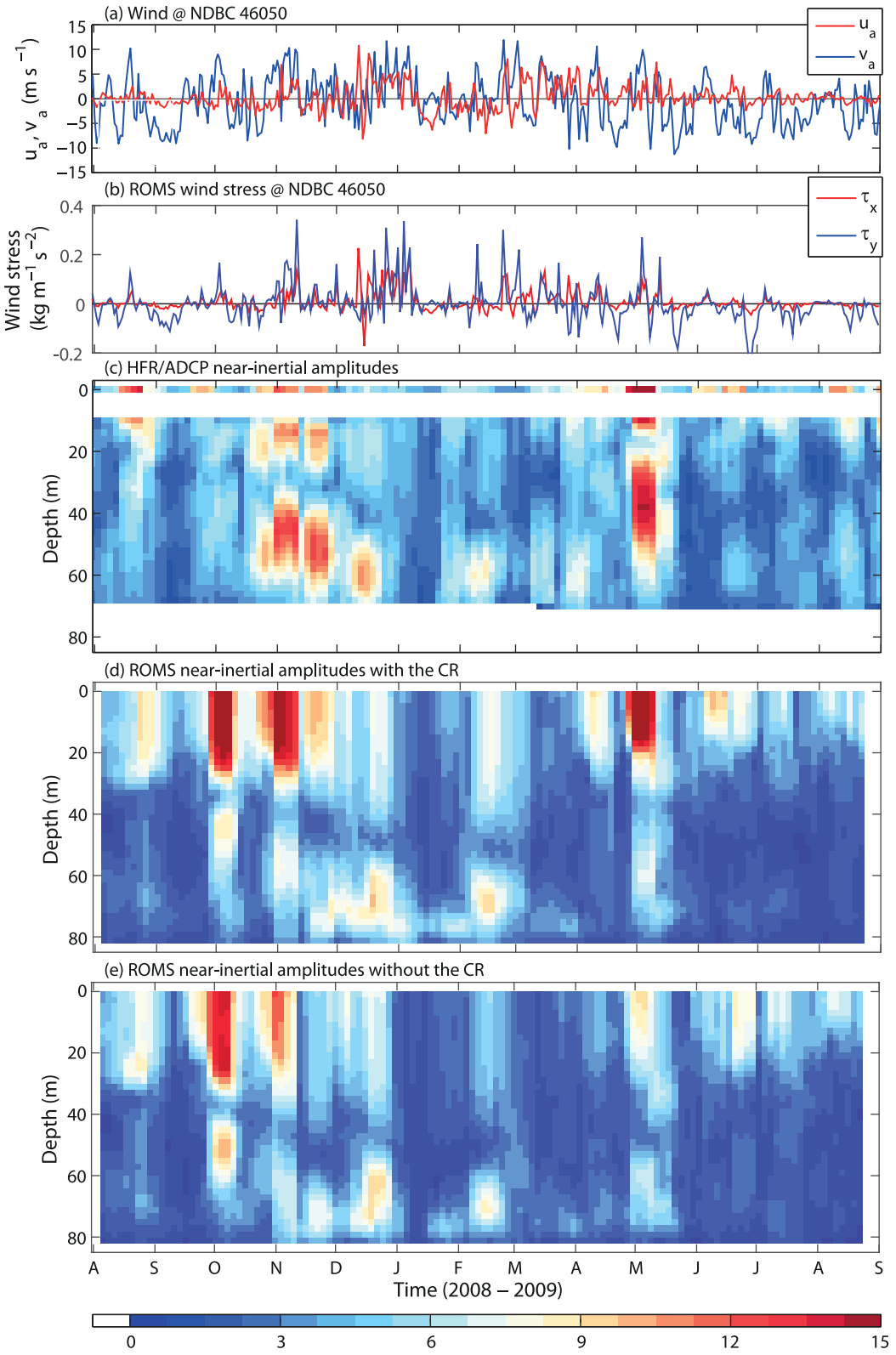

Figure 5. (a) Daily averaged time series of east-west (u_a) and north-south (v_a) wind components and (b) ROMS wind stress (τ_x and τ_y) at the NDBC 46050 buoy (W at Figure 1). (c) Clockwise near-inertial amplitudes (cm s^{-1}; -1.555 cpd $\leq \sigma^- \leq -1.255$ cpd) obtained from the observed surface currents (HFR) and subsurface current profiles (ADCP) at the NH10 mooring location. The individual estimates are computed using a moving time window of 12 days with an increment of 3 days. (d and e) Clockwise near-inertial amplitudes at the same location obtained from ROMS simulations with the CR ($A_{\cdot}^{-}$) and without the CR ($A_{\circ}^{-}$), respectively.

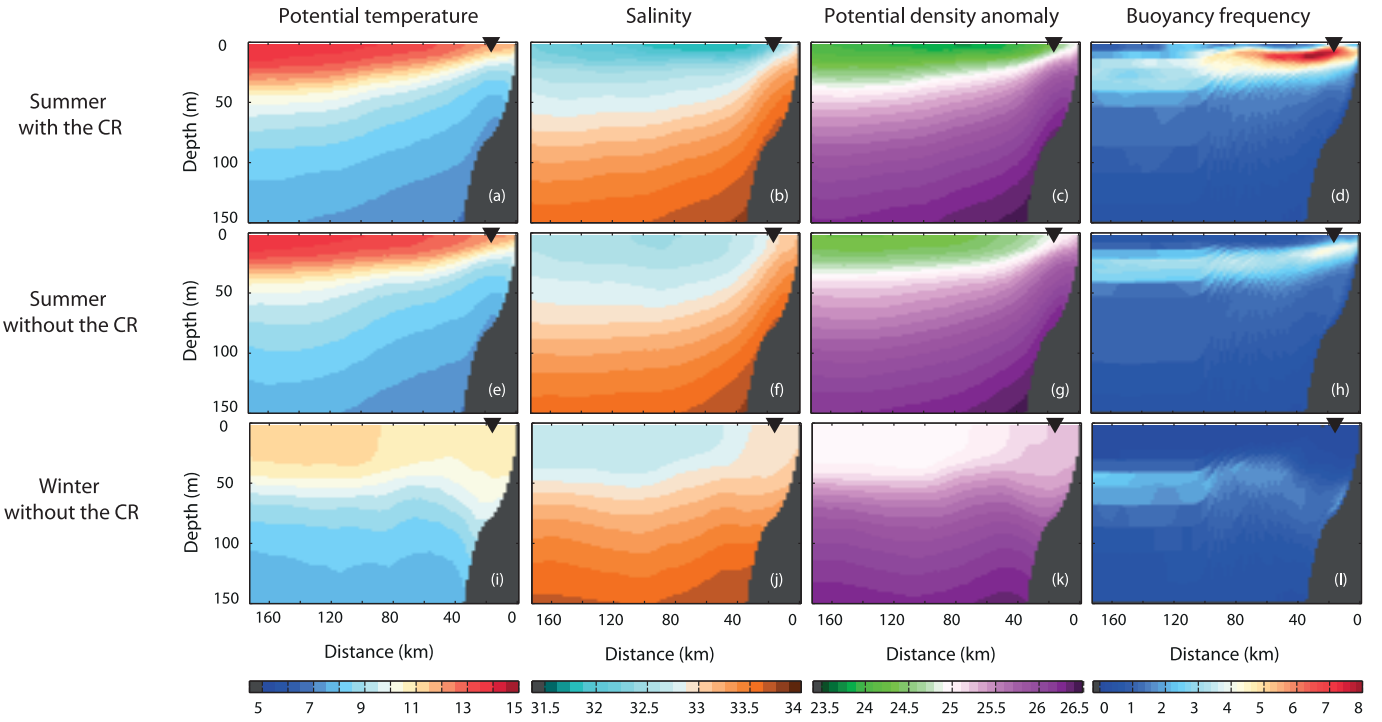

Figure 6. Conditionally averaged potential temperature (°C), salinity, potential density anomaly ($\rho\prime(l,z)=\rho(l,z)-1000$; kg m^{-3}), and buoyancy frequency ($\times 10^4$, s^{-2}) obtained from ROMS simulations under three cases. (a–d) Summer with the CR. (a) $T_{\cdot,S}$, (b) $S_{\cdot,S}$, (c) $\rho'_{\cdot,S}$, and (d) $N^2_{\cdot,S}$. (e–h) Summer without the CR. (e) $T_{\circ,S}$, (f) $S_{\circ,S}$, (g) $\rho'_{\circ,S}$, and (h) $N^2_{\circ,S}$. (i–l) Winter without the CR. (i) $T_{\circ,W}$, (j) $S_{\circ,W}$, (k) $\rho'_{\circ,W}$, and (l) $N^2_{\circ,W}$.

3. Results

The statistics of the coastal near-inertial currents are presented as the entire year average (and time series for the entire year) and three conditional averages—(1) summer with the CR, (2) summer without the CR, and (3) winter without the CR—in the form of horizontal maps and cross-shore sections. Based on the analysis of observed and model stratification and wind stress (Figures 4 5a, 5b, and 6), the summer and winter time windows for spectral analyses are referred to as April–October 2009 and November 2008 to March 2009, respectively. The corresponding three cases of conditionally averaged cross-shore transects of potential temperature, salinity, potential density anomaly, and buoyancy frequency are shown in Figure 6.

3.1. Subsurface and Surface Near-Inertial Amplitudes

The time series of the daily averaged cross-shore and alongshore wind at the NDBC 46050 buoy (15 km offshore of the mooring NH10) and the daily averaged ROMS wind stress components at the NH10 mooring location show seasonal variability, including predominantly poleward storm events during winter and persistent equatorward wind conditions during spring and early summer (Figures 5a and 5b).

The amplitude of currents (A^- and A^+) in the clockwise and counter-clockwise near-inertial frequency bands ($\hat{\sigma}^{\pm}$) is presented as a function of depth (z) or cross-shore direction (l) or both:

$$A^{\pm}(l,z)=\left[\int_{\hat{\sigma}^{\pm}} S_{\mathbf{u}}(l,z,\hat{\sigma}^{\pm})\mathrm{d}\sigma\right]^{\frac{1}{2}}. \tag{3}$$

The near-inertial frequency band ($\hat{\sigma}^{\pm}$) is defined as the local inertial frequency (f_c) with a bandwidth of 0.3 cpd. The negative ($^-$) and positive ($^+$) superscripts refer to clockwise and counter-clockwise rotations, respectively. For instance, the clockwise near-inertial frequency band ($\hat{\sigma}^-$) at the NH line is equal to -1.555 cpd $\leq\sigma\leq -1.255$ cpd.

The temporal variability of near-inertial currents at the mooring location is presented with time series of the clockwise near-inertial amplitudes computed with a box-car average using a moving time window of 12 days with an increment of 3 days (Figures 5c). The estimates from the HFR-derived surface currents are

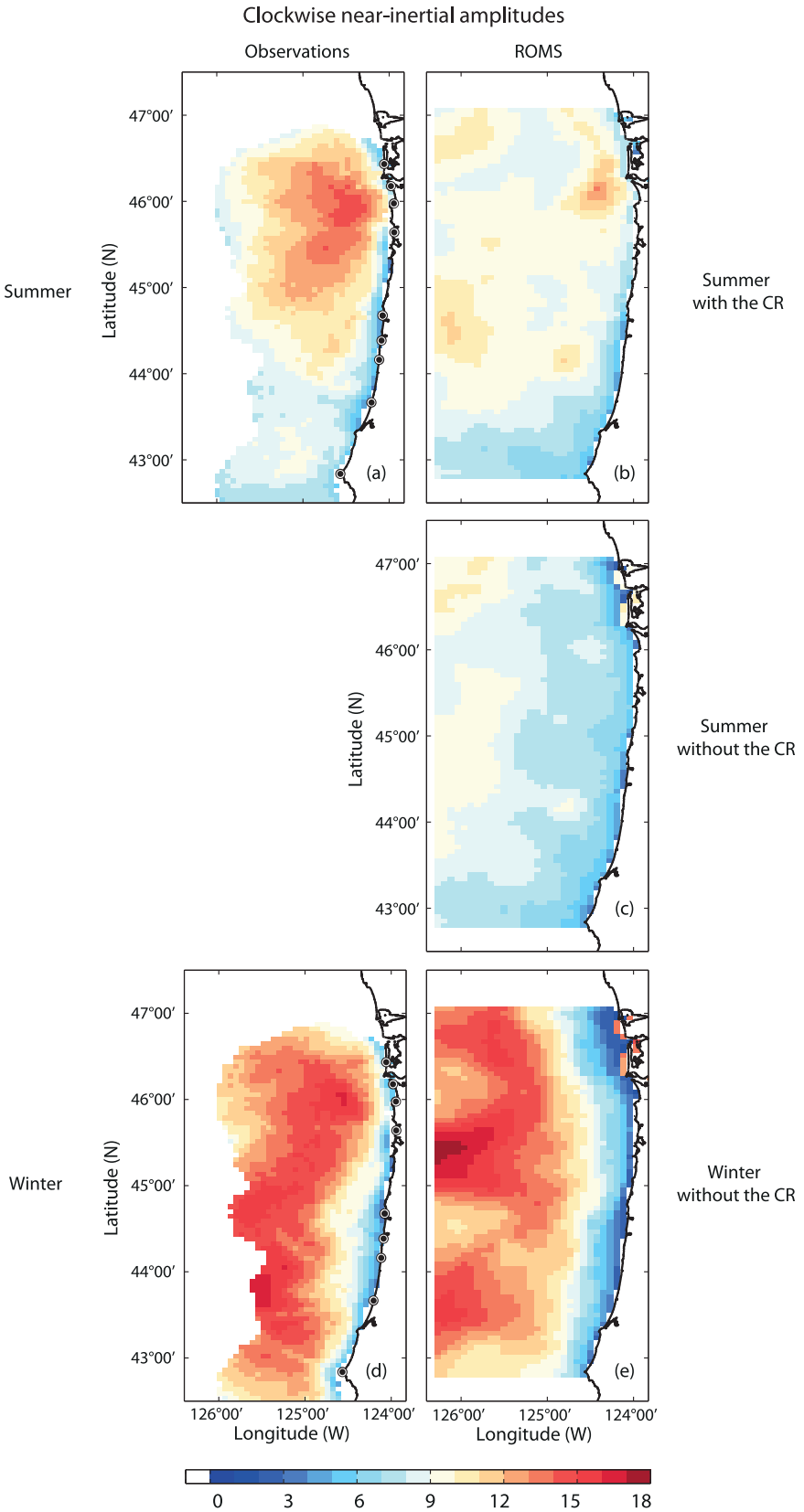

Figure 7. Seasonally (conditionally) averaged amplitudes (cm s^{-1}) of surface (layer) currents, using HFR observations and ROMS simulations, in the clockwise near-inertial frequency band (-1.555 cpd $\leq \sigma^{-} \leq -1.255$ cpd). (a and d) HFR-derived surface currents. (b, c, and e) ROMS simulations at the surface layer. (a–c) Summer. (d and e) Winter. (a) A^{-}_{S}, (b) $A^{-}_{,S}$, (c) $A^{-}_{\circ S}$, (d) A^{-}_{W}, and (e) $A^{-}_{\circ W}$.

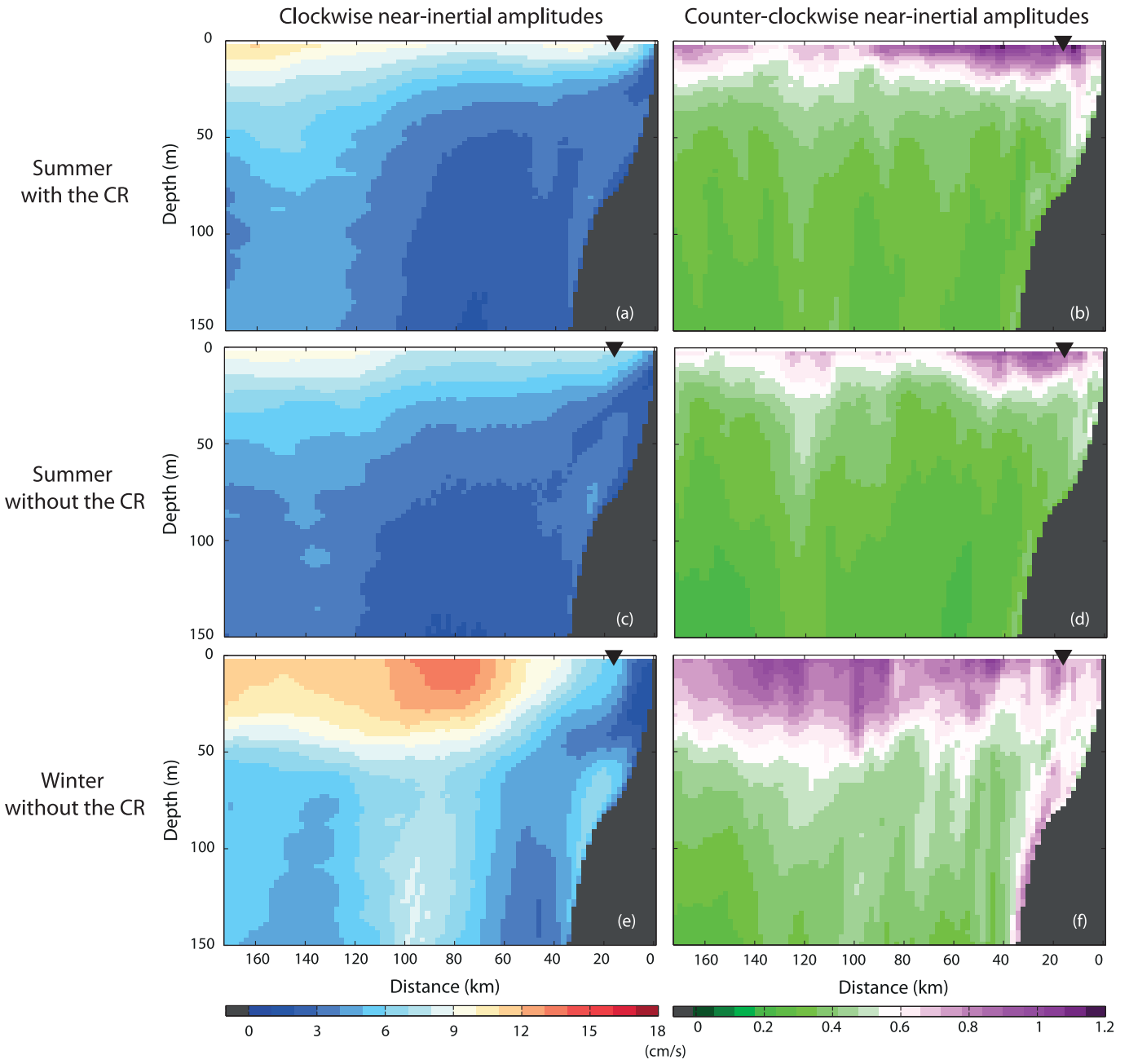

Figure 8. Conditionally averaged amplitudes (cm s^{-1}) of subsurface currents, using ROMS simulations, on the NH line in the (a, c, and e) clockwise (-1.555 cpd $\leq \sigma^{-} \leq -1.255$ cpd) and (b, d, and f) counter-clockwise (1.255 cpd $\leq \sigma^{+} \leq$ 1.555 cpd) near-inertial frequency bands. (a) $A^{-}_{\bullet,S}$, (b) $A^{+}_{\bullet,S}$, (c) $A^{-}_{\circ,S}$, (d) $A^{+}_{\circ,S}$, (e) $A^{-}_{\circ,W}$, and (f) $A^{-}_{\circ,W}$. The location of the NH10 mooring location is marked as a black triangle.

shown at the top of the water column. Events of intensified wind stress can be found preceding each interval of the enhanced near-inertial currents. In December 2008, the near-inertial response is amplified near bottom, below 50 m, when the upper water column over the shelf is unstratified due to downwelling and mixing (see Figure 6i).

The near-inertial currents at the mooring location obtained from ROMS simulations with and without the CR ($\mathbf{u}_{\bullet}$ and $\mathbf{u}_{\circ}$) are presented in the same way (Figures 5d and 5e). The amplitudes of near-inertial currents with the CR in the upper 20 m are 20%–30% enhanced compared with the near-inertial currents without the CR because of the stronger stratification in the upper layer (Figures 4f and 4i). The timing with which

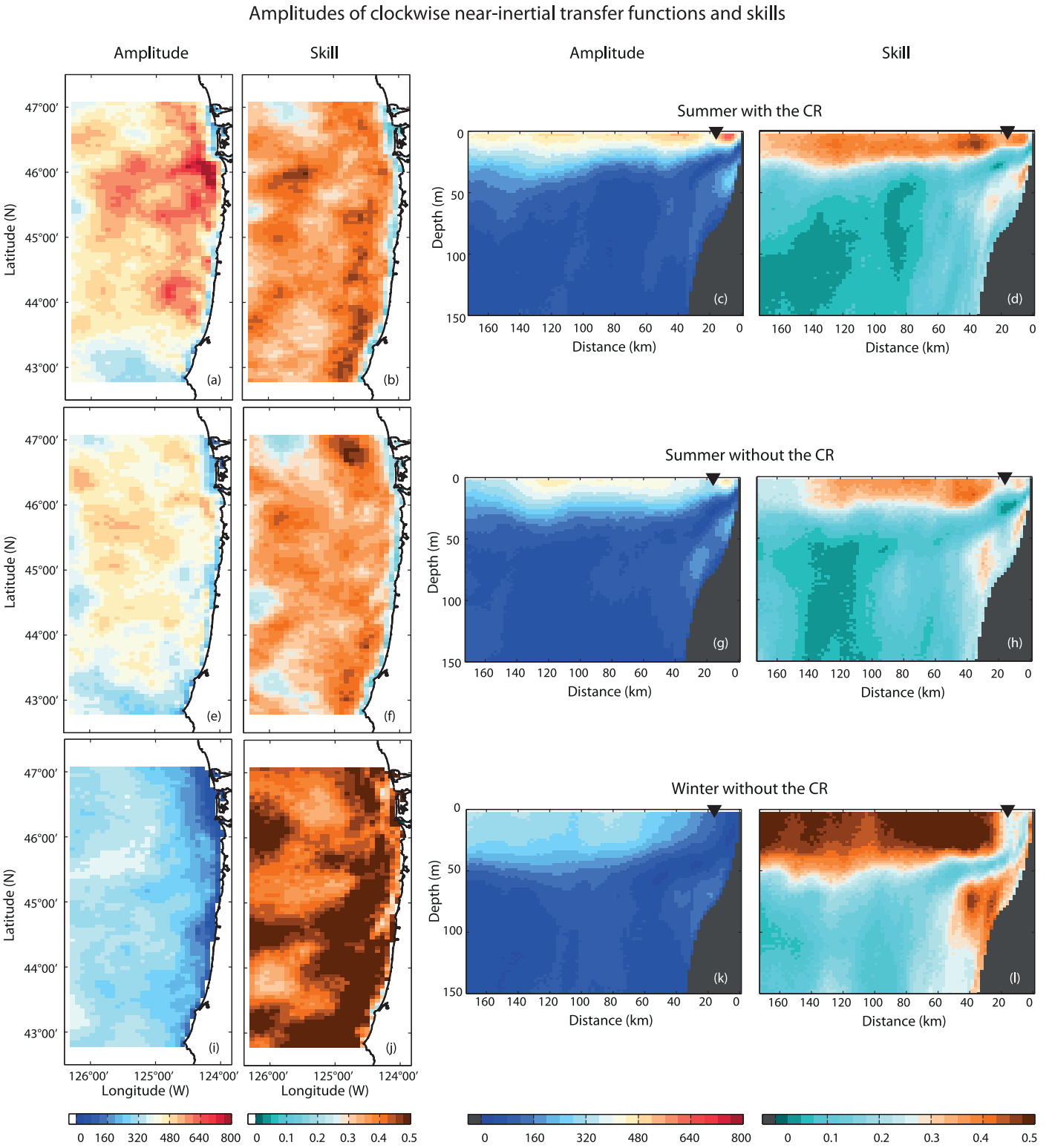

Figure 9. Conditionally estimated amplitudes ($|\overline{\mathbf{H}}|$, $kg^{-1}\ m^2\ s$) of transfer functions and skills (κ, dimensionless) in the clockwise near-inertial frequency band, using ROMS simulations, are presented as a surface map and a cross section along a cross-shore line. (a and c) $|\overline{\mathbf{H}}_{\cdot,S}|$, (b and d) $\kappa^2_{\cdot,S}$, (e and g) $|\overline{\mathbf{H}}_{\circ,S}|$, (f and h) $\kappa^2_{\circ,S}$, (i and k) $|\overline{\mathbf{H}}_{\circ,W}|$, and (j and l) $\kappa^2_{\circ,W}$. The amplitude is the value averaged over the near-inertial frequency band. The NH10 mooring is located 18 km from the shoreline, marked as a downward black triangle.

significant near-inertial currents appear is nearly consistent with observations except for an event only in both model simulations (Figures 5c–5e). Both observed (Figure 5c) and model (Figures 5d and 5e) near-inertial clockwise current amplitudes are enhanced near surface and shelf bottom and exhibit minimum between 20 and 60 m, near the base of the surface mixed layer.

As mentioned in section 1, one would expect stronger surface near-inertial currents in presence of stronger stratification, given the same wind stress. Off Oregon, stratification is stronger in summer and winds are dominant in winter. So it is not a priori clear which season would experience stronger inertial motions. The amplitudes of the clockwise near-inertial currents observed by the HFR in summer (Figure 7a) on average over the study domain are weaker than those in winter (Figure 7d). In the area of the CR plume, the summer inertial currents are locally intensified and are more comparable to the amplitude of the winter inertial currents. The model reproduces well the intensity of the near-inertial currents in winter (Figures 7d and 7e). The model response in summer is weaker than observed in the area of the CR plume (Figures 7a and 7b). Still, the model with the CR yields increased near-inertial current amplitudes compared to the case without the CR (Figure 7c). In all the plots we see the decreased inertial clockwise motions near coast. In winter, this area becomes wider than in summer, in part due to the low stratification on the shelf (see Figure 6).

As seen in the NH cross-shore sections (Figures 8a and 8c), the amplitudes of clockwise near-inertial currents simulated with the CR ($A^{-}_{\bullet,S}$) are enhanced in the upper 100 m and are approximately twice as high as those modeled without the CR ($A^{-}_{\circ,S}$), as the momentum injected by wind stress is better trapped in the surface layer by the stronger stratification (Figure 6d) than with a well-mixed water column or reduced stratification. The amplitudes of counter-clockwise near-inertial currents ($A^{+}_{\bullet,S}$ and $A^{+}_{\circ,S}$) are much smaller and are enhanced near the coast compared to offshore as the rectilinear motions should be expected near the coast (Figures 8b and 8d). In general, above 500 m depth, there is persistent upward phase propagation in the offshore region, which indicates downward energy propagation, possibly caused by wind stress (not shown) [e.g., *Rainville and Woodgate*, 2009]. The near-inertial amplitudes during winter ($A^{-}_{\circ,W}$) are enhanced and found in a thicker layer as the wind events are stronger than in summer (Figure 8e).

3.2. Primary Contributions to Near-Inertial Currents

3.2.1. Wind Transfer Function and Skill Definitions

The wind transfer function (**H**) is estimated using time series of the paired ROMS wind stress and ROMS currents at the surface layer (the first column in Figure 9), the cross-shore line (the third column in Figure 9), and the mooring location (Appendix A). In other words, a single basis function (e.g., wind stress) colocated in the horizontal location with the currents is used in this frequency domain regression analysis. The wind transfer functions are presented as the averaged value ($\overline{\mathbf{H}}^{\pm}$) within the near-inertial frequency band ($\hat{\sigma}^{\pm}$) (section 3.2.2). Its amplitude ($|\overline{\mathbf{H}}^{\pm}|$) and phase ($\Theta^{\pm}$) are given by

$$\overline{\mathbf{H}}^{\pm}(x,y)=\frac{1}{n}\sum_{\hat{\sigma}^{\pm}}|\mathbf{H}(x,y,\hat{\sigma}^{\pm})|, \tag{4}$$

$$=|\overline{\mathbf{H}}^{\pm}(x,y)|e^{i\Theta^{\pm}(x,y)}, \tag{5}$$

where n is the number of frequency bins. The wind transfer function is defined as

$$\mathbf{H}(x,y,\sigma)=\frac{\langle\hat{\mathbf{u}}(x,y,\sigma)\hat{\boldsymbol{\tau}}^{\dagger}(x,y,\sigma)\rangle}{\langle\hat{\boldsymbol{\tau}}(x,y,\sigma)\hat{\boldsymbol{\tau}}^{\dagger}(x,y,\sigma)\rangle+\langle\boldsymbol{\epsilon}\boldsymbol{\epsilon}^{\dagger}\rangle}, \tag{6}$$

where $\hat{\mathbf{u}}$ and $\hat{\boldsymbol{\tau}}$ are Fourier coefficients of currents and wind stress at the same horizontal location (x, y), respectively, and $\langle\boldsymbol{\epsilon}\boldsymbol{\epsilon}^{\dagger}\rangle$ is the noise covariance of wind stress (see Kim et al. [2009a, 2014, 2015] for more details on the transfer function analysis). The symbol† denotes the complex conjugate transpose. The eight primary tidal constituents (M_2, S_2, K_1, O_1, K_2, N_2, P_1, and Q_1) are removed by least squares fitting prior to estimating the transfer functions. An example of the wind transfer function estimated from observations (e.g., winds and ADCP) and ROMS outputs (e.g., model winds and currents) at the NH10 mooring location on the Oregon midshelf is shown in Appendix A.

The skill (κ) is defined as the fraction of the variance explained by the transfer function [e.g., *Kim et al.*, 2009a]:

$$\kappa = 1 - \frac{\langle [\hat{\mathbf{u}}(x,y,\sigma) - \mathbf{H}(x,y,\sigma)\hat{\boldsymbol{\tau}}(x,y,\sigma)]^2 \rangle}{\langle \hat{\mathbf{u}}^2(x,y,\sigma) \rangle}. \quad (7)$$

Zero skill means that the variance of residuals from the fit is as large as the original variance, i.e., the process cannot be described at all as driven by the winds.

Since the regression analysis using a single basis function can capture the local wind variability better than the remotely forced wind variance [e.g., *Kim*, 2014], the residual of regression may contain the remotely forced variability. Moreover, the variance due to nonlinear interactions of currents which are not directly dependent on the wind stress may not be isolated with the wind transfer function analysis.

3.2.2. Influence of Riverine Waters

The influence of freshwater inputs from the CR on the clockwise near-inertial currents is presented with the relative difference (α) of amplitudes of transfer functions with and without the CR ($\overline{\mathbf{H}}_{\bullet,S}$ and $\overline{\mathbf{H}}_{\circ,S}$) using model simulations during summer:

$$\alpha^{-}(x,y) = \frac{||\overline{\mathbf{H}}^{-}_{\circ,S}(x,y)| - |\overline{\mathbf{H}}^{-}_{\bullet,S}(x,y)||}{|\overline{\mathbf{H}}^{-}_{\circ,S}(x,y)|}. \quad (8)$$

Similarly, $\alpha^{\pm}(l,z)$ can be defined for a cross-shore vertical section.

The wind transfer functions in the clockwise near-inertial frequency band ($\overline{\mathbf{H}}^{-}_{\bullet,S}$ and $\overline{\mathbf{H}}^{-}_{\circ,S}$) computed from two ROMS simulations with and without the CR under the summer seasonal stratification are presented as a surface map and a cross-shore section to examine the influence of freshwater inputs from the CR as the wind-current responses averaged over summer. These characterize the structure of the direct and local responses of the ocean to the winds.

The amplitudes of transfer functions with the CR are enhanced compared to those without the CR (Figures 9a and 9e). The relative difference between transfer functions with and without the CR (α^{-}; Figure 10a) is approximately 0.5 near the coast, in particular near the CR, and is reduced to 0.1 farther from the CR in both cross-shore and alongshore directions, which can be related to the freshwater footprints from the CR (Figure 6). The spatial pattern of the ratio map is close to the spatial distribution of the summer-averaged surface potential density (Figures 10c and 10d). Note that the difference of surface density can be an indicator to present the stratification in the upper layer as the freshwater discharges or river runoffs tend to spread in the upper layer [e.g., *Hickey et al.*, 2005; *Warrick et al.*, 2007; *Kim et al.*, 2009b]. The spatial distribution of the time mean surface potential density changes abruptly near the CR mouth within 5 kg m^{-3} and smoothly offshore within 1 kg m^{-3} (Figures 10c and 10d). In our interpretation, stronger stratification yields the enhanced near-inertial response given the same wind stress. Thus, the stratified condition associated with the CR leads to 30%–60% stronger near-inertial motions. The skill (κ; equation (7)) has a similar order of amplitude both with and without the CR (Figures 9b and 9f; $\kappa_{\bullet,S} \approx \kappa_{\circ,S}$).

In the same manner, the transfer functions estimated from the two simulations are compared in the cross-shore direction (Figures 9c and 9g). The amplitudes of transfer functions become reduced with depth and nearshore, where the influence of coastal boundary conditions on the near-inertial currents becomes dominant. The amplitudes and phases of transfer functions exhibit a consistent structure in the cross-shore direction (Figures 11b, 11d, and 11f). The near-inertial variance explained by wind stress in the two simulations does not change substantially.

As the chosen cross-shore section line (Figures 9d and 9h) is located approximately 130 km south of the CR, the direct influence of the CR may be diluted to some degree. Nonetheless, the amplitudes of transfer functions in the upper 50 m are 20%–30% enhanced due to the varying stratification. The vertical and cross-shore distributions of near-inertial variance skillfully explained with direct wind stress are nearly the same in both cases or slightly shallower in the case with the CR than the one without the CR.

3.2.3. Influence of Seasonal Conditions

The influence of seasonal heat fluxes on the clockwise near-inertial currents can be quantified with the relative difference (β) of amplitudes of transfer functions during summer ($\overline{\mathbf{H}}_{\circ,S}$) and winter ($\overline{\mathbf{H}}_{\circ,W}$) using model simulations without the CR:

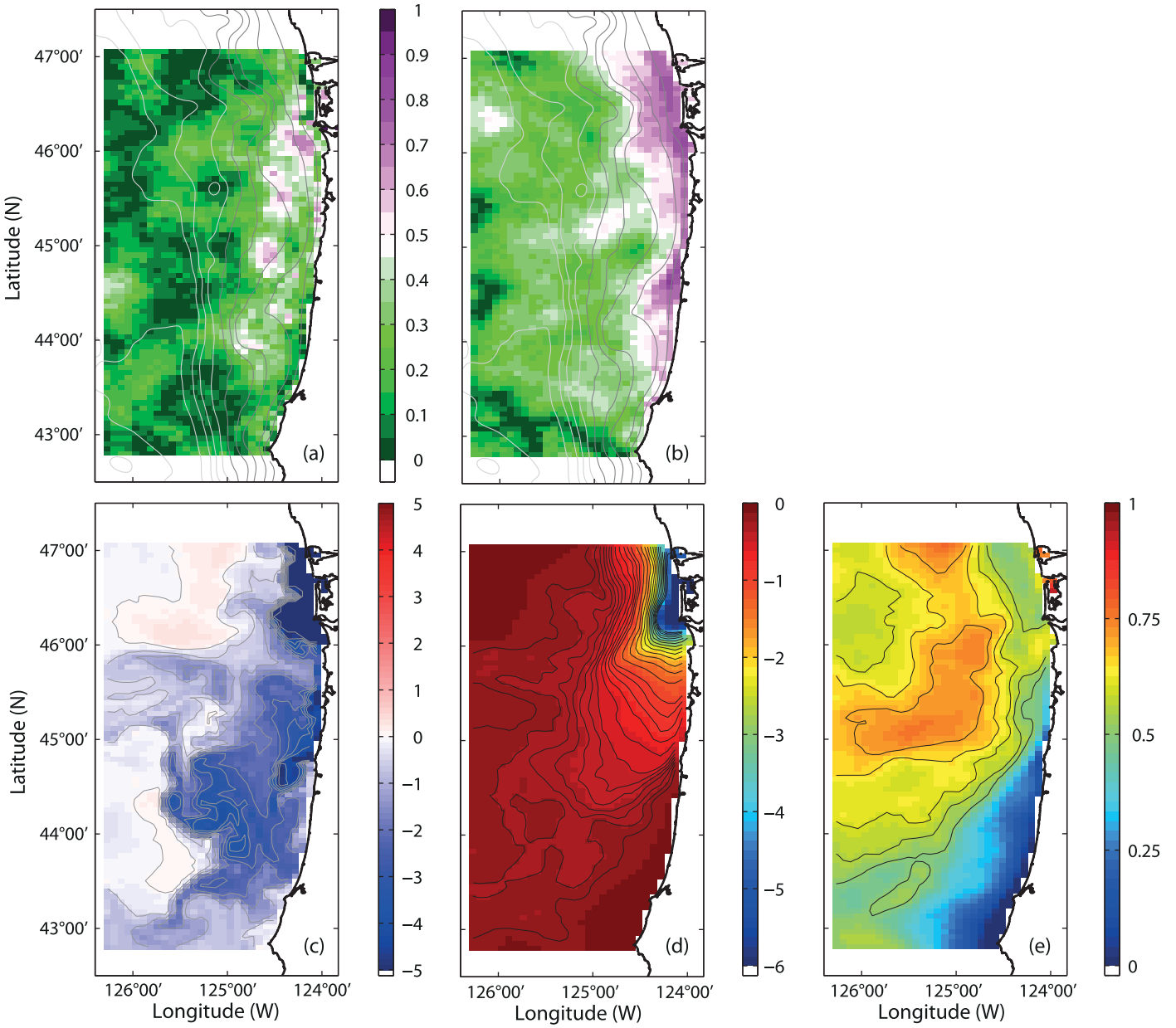

Figure 10. (a and b) Relative differences of the amplitude of the transfer functions. (a) α^-. (b) β^-. Note that Figures 10a and 10b share a color bar, and the gray contours indicate the isobath lines of 50, 100, 250, 500, 1000, 1500, 2000, 2500, 3000, 3500, and 4000 m. (c–e) Surface potential density map (kg m^{-3}). (c) Difference between the surface potential density of two simulations ($\Delta\rho = \rho_{\cdot} - \rho_{\circ}$) at the time when the freshwater footprint is prevalent (9 June 2009 (GMT); see Figure 4l). (d) Difference of surface potential density of two simulations averaged over summer ($\Delta\rho_2 = \rho_{\cdot,S} - \rho_{\circ,S}$). (e) Difference between the seasonally averaged potential density of a simulation without the CR ($\Delta\rho_3 = \rho_{\circ,W} - \rho_{\circ,S}$).

$$\beta^-(x,y) = \frac{||\overline{\mathbf{H}}^-_{\circ,S}(x,y)| - |\overline{\mathbf{H}}^-_{\circ,W}(x,y)||}{|\overline{\mathbf{H}}^-_{\circ,S}(x,y)|}. \quad (9)$$

The wind transfer functions in the clockwise near-inertial frequency band ($\overline{\mathbf{H}}^-_{\circ,S}$ and $\overline{\mathbf{H}}^-_{\circ,W}$), computed from observations (three NDBC wind buoys and HFR-derived surface currents) and ROMS simulations (currents and wind stress) without the CR, are presented as a cross-shore section (ROMS only) (Figures 9i–9l) and a surface map (Figure 12) to investigate the influence of seasonal heat fluxes.

In contrast to the difference in amplitudes of seasonal near-inertial surface currents (Figures 7 and 8), the HFR-derived summer transfer functions are approximately enhanced by 50% compared to the winter

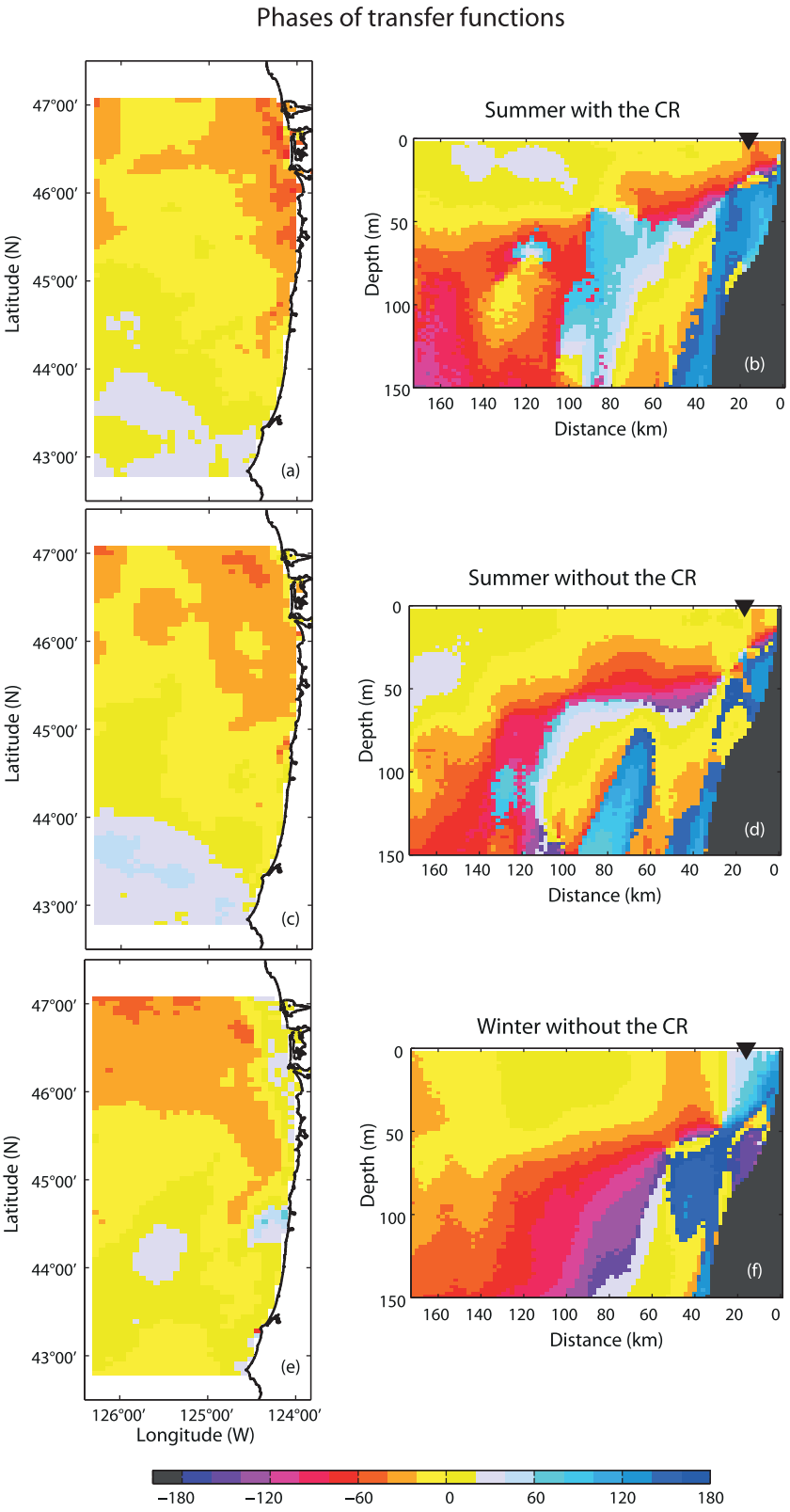

Figure 11. Conditionally estimated phases (Θ, degrees) of transfer functions, using ROMS simulations, in the clockwise near-inertial frequency band are presented as a surface map and a cross section along a cross-shore line. (a and b) $\Theta_{\cdot,S}$, (c and d) $\Theta_{\cdot,S}$, and (e and f) $\Theta_{\cdot,W}$. The phase is the value at the inertial frequency. The NH10 mooring location is located 18 km from the shoreline, marked as a downward black triangle.

transfer functions (Figures 12a–12f), depending on location of wind buoys as a footprint of effective wind forcing [cf. *Kim et al*., 2014, Figures 11 and 12]. The winter skills are higher than summer skills as the seasonal wind events to generate near-inertial surface currents are more dominant (have higher signal-to-noise ratio) during winter than summer (Figures 12g–12l). The residual may contain some portion of remotely forced wind variance and baroclinic tidal currents, which can be noise in the context of wind regression analysis [e.g., *Kim*, 2014]. Similarly, the amplitudes of the model-derived summer transfer function in the clockwise near-inertial frequency band are 20%–70% greater than those of the winter transfer function (Figures 9i and 9k).

The winter wind skill varies from 30% to 70%, which is larger than the summer wind skill, indicating a larger fraction of the current variance from directly wind-forced near-inertial surface currents during winter compared to summer (Figures 9f and 9j). The relative difference between transfer functions in summer and winter (β^{-}) is approximately 0.7 near the coast (Figure 10b), which is associated with less stratified conditions on the shelf (Figures 6i–6l and 10e).

The amplitudes of the summer transfer function along the chosen cross-shore line are 20%–70% enhanced compared with those of the winter transfer function (Figures 9g and 9k). The penetration depth of wind stress is approximately twice as deep in winter as in summer (Figures 9h and 9l), consistent with the increase in the mixed-layer depth, and the near-inertial variance in winter is approximately 70% better explained by local winds than in summer (Figures 9h and 9l).

3.3. Coastal Inhibition

The coastal inhibition of near-inertial currents is manifested in their downward energy flux from the surface-coast corner, i.e., upward and offshore phase propagation near the coast [e.g., *Pettigrew*, 1981; *Kim et al*., 2014]. In this section, the subsurface structures of clockwise near-inertial currents using ROMS outputs are examined with spatial coherence and ray tracing.

The study of cross-shore coherence within the frequency band of interest and ray tracing of individual frequencies of interest can be ways to investigate the phase propagation of internal motions (e.g., near-inertial internal waves), which can present coastal inhibition in an intuitive manner showing cross-shore variation of horizontal and vertical length scales and phases, consistent with asymmetric near-inertial currents at the coastal boundaries [e.g., *Leaman and Sanford*, 1975; *D'Asaro and Perkins*, 1984; *Zervakis and Levine*, 1995].

3.3.1. Spatial Coherence

The spatial coherence ($\hat{c}$), or the spatial correlation within a specific frequency band [e.g., *Emery and Thomson*, 1997; *Kim and Kosro*, 2013; *Kim et al*., 2014], has been used to examine the spatial structure of variability in a given frequency band ($\hat{\sigma}$). Its magnitude ($|\hat{c}|$) and phase (θ) are presented as a function of spatial lags of the cross-shore distance (Δl) and depth (Δz) from the given reference location (l, z):

$$\hat{c}(\Delta l,\Delta z)=\frac{\langle \hat{\mathbf{u}}(l,z,\hat{\sigma})\ \hat{\mathbf{u}}^{\dagger}(l+\Delta l,z+\Delta z,\hat{\sigma})\rangle}{\sqrt{\langle|\hat{\mathbf{u}}(l,z,\hat{\sigma})|^2\rangle}\sqrt{\langle|\hat{\mathbf{u}}(l+\Delta l,z+\Delta z,\hat{\sigma})|^2\rangle}}\ , \tag{10}$$

$$=|\hat{c}(\Delta l,\Delta z)|e^{i\theta(\Delta l,\Delta z)}, \tag{11}$$

where $\hat{\mathbf{u}}(l,z)$ is the Fourier coefficient of current time series at a given cross-shore location (l) and depth (z), and $\langle\cdot\rangle$ indicates averaging over the near-inertial frequency band ($\hat{\sigma}$). Negative (positive) phases indicate that the physical variable at the reference location leads (follows) the target physical variable at the location with spatial lags.

The spatial coherence of the full-year currents (**u.**) in the clockwise near-inertial frequency band along the cross-shore line is presented with its amplitudes and phases at eight different cross-shore locations and depths: four locations at the near-surface and subsurface, respectively. The four near-surface locations are located within 40 km from the coast to present the coastal inhibition in the near-coast and surface regions (Figures 13a–13d and 13j–13m). A magnified view of coastal inhibition is shown in Figures 13i and 13r. Moreover, the four subsurface locations are divided into two nearshore locations (within 40 km from the shore) at 30 m depth (Figures 13e, 13f, 13n, and 13o) and two offshore locations at 80 m depth (Figures 13g, 13h, 13p, and 13q), which are chosen to highlight the length scales (amplitudes) and propagation features (phases) of clockwise near-inertial currents in the cross-shore direction.

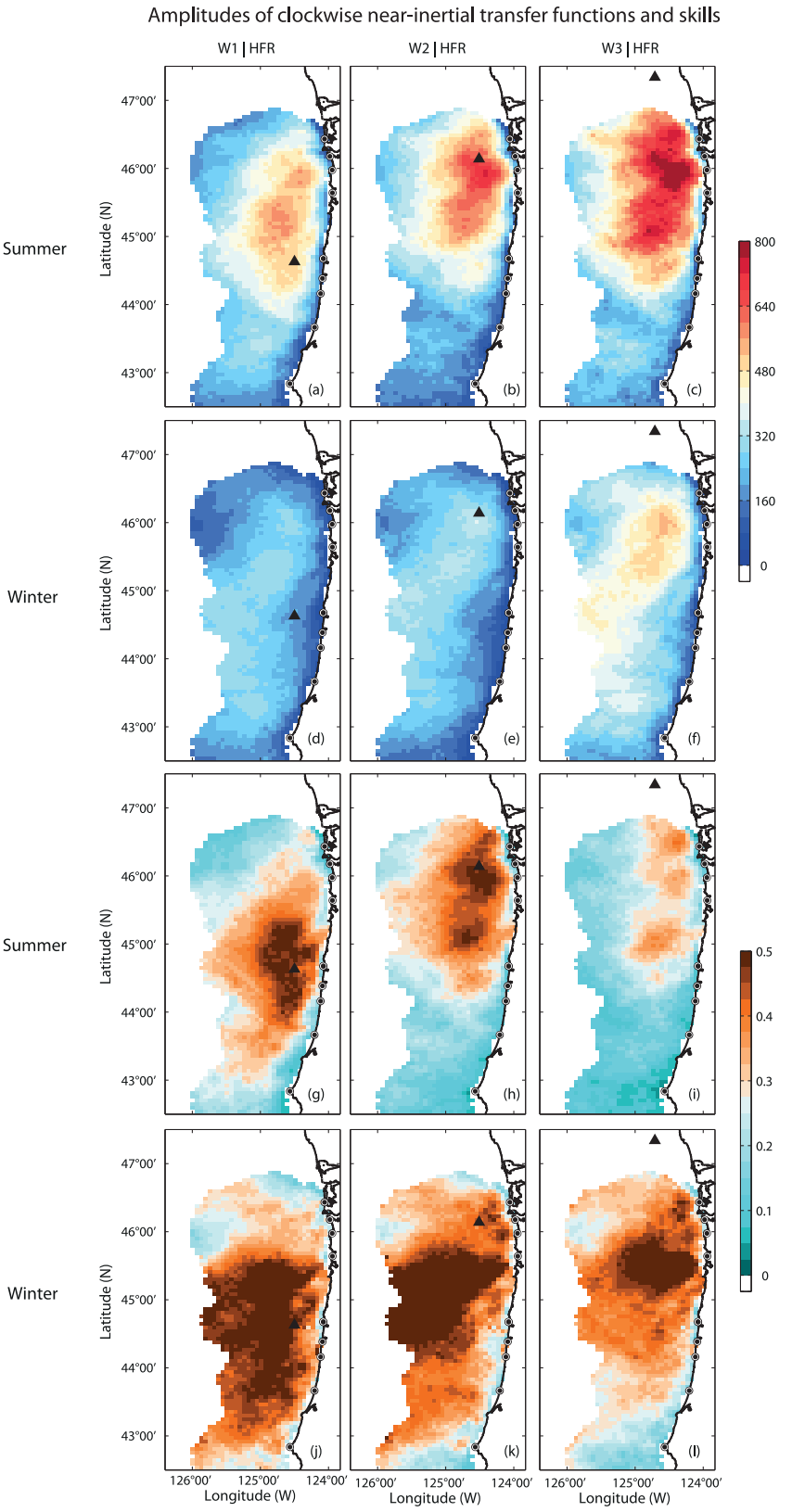

Figure 12. Seasonally estimated amplitudes ($|\overline{\mathbf{H}}|$, kg^{-1} m^2 s) of transfer functions and skills (κ, dimensionless), using NDBC winds (46050 (W1), 46029 (W2), and 46041 (W3)) and HFR-derived surface currents, in the clockwise near-inertial frequency band. Individual wind buoys are marked with black triangles. (a–f) Amplitudes. (a) $|\overline{\mathbf{H}}_{W1,S}|$, (b) $|\overline{\mathbf{H}}_{W2,S}|$, (c) $|\overline{\mathbf{H}}_{W3,S}|$, (d) $|\overline{\mathbf{H}}_{W1,W}|$, (e) $|\overline{\mathbf{H}}_{W2,W}|$, and (f) $|\overline{\mathbf{H}}_{W3,W}|$. (g–l) Skills. (g) $\kappa_{\overline{W1,S}}$, (h) $\kappa_{\overline{W2,S}}$, (i) $\kappa_{\overline{W3,S}}$, (j) $\kappa_{\overline{W1,W}}$, (k) $\kappa_{\overline{W1W}}$, and (l) $\kappa_{\overline{W3,W}}$.

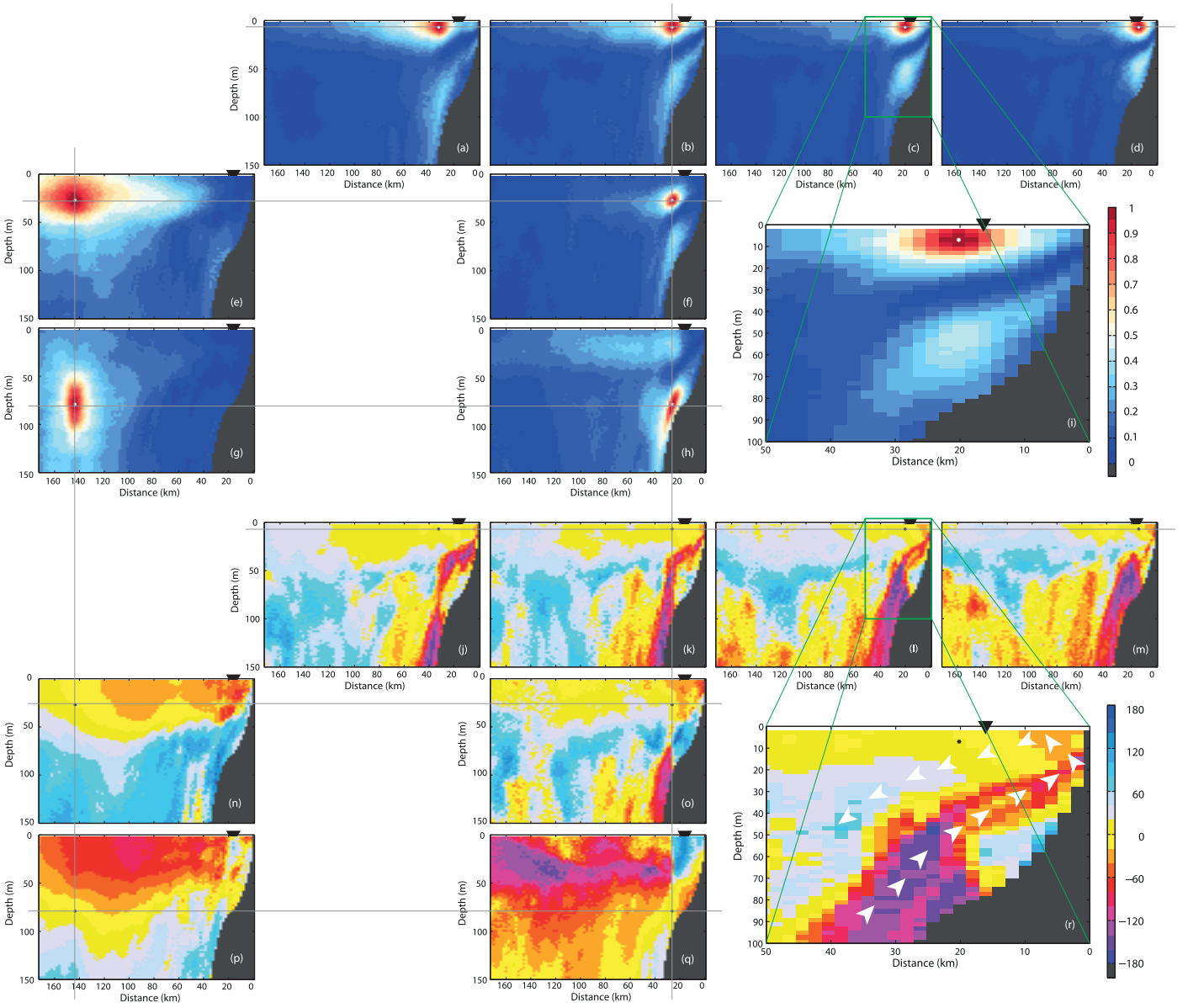

Figure 13. Magnitudes ($|\dot{c}^{-}_{\star}|$) and phases ($\theta^{-}_{\star}$, degrees) of the spatial coherence of ROMS currents with the CR (**u**.) for the entire year in the clockwise near-inertial frequency band relative to a reference location (black or white stars) along a cross-shore line. (a–d and j–m) Four grid points near the surface and coast. (e, f, n, and o) Offshore and nearshore, two grid points each, in the upper layer. (g, h, p, and q) Offshore and nearshore, two grid points each, in the lower layer. (i and r) Magnified views in the nearshore region of Figures 13c and 13l (green boxes), respectively. Gray horizontal and vertical lines denote the same location of reference points in the cross-shore direction and depth. The NH10 mooring location is located 18 km from the shoreline, marked as a downward black triangle. White arrowheads in Figure 13r indicate the increasing direction of phase: The phase propagates upward over the continental shelf, reflects at the coast, and then increases upward offshore and downward offshore at the sea surface.

The length scales of clockwise near-inertial near-surface currents increases offshore and decrease onshore (Figures 13a–13d), consistent with *Kim et al.* [2014, Figure 8]. The clockwise near-inertial currents show more coherent horizontal motions in the upper layer (above 50 m depth) than those in the lower layer (below 50 m depth) considering the aspect ratio of the cross-shore section (Figures 13e–13h). Comparing the amplitudes of coherence of the near-inertial currents over the continental shelf and deep water (Figures 13g and 13h), the length scales more quickly decrease near the coast than the phase at the near-surface (Figures 13a–13d).

The pattern of the phase propagation in the offshore region (see Figures 13n and 13p) is upward, consistent with the result of a one-dimensional analytical model and typical patterns of inertial motion's propagations in the presence of the density gradient in the cross-shore direction [e.g., *Krauss*, 1972, 1979; *D'Asaro and Perkins*, 1984; *D'Asaro*, 1985]. Considering the spatial variation of the phase in a region within 40 km from the

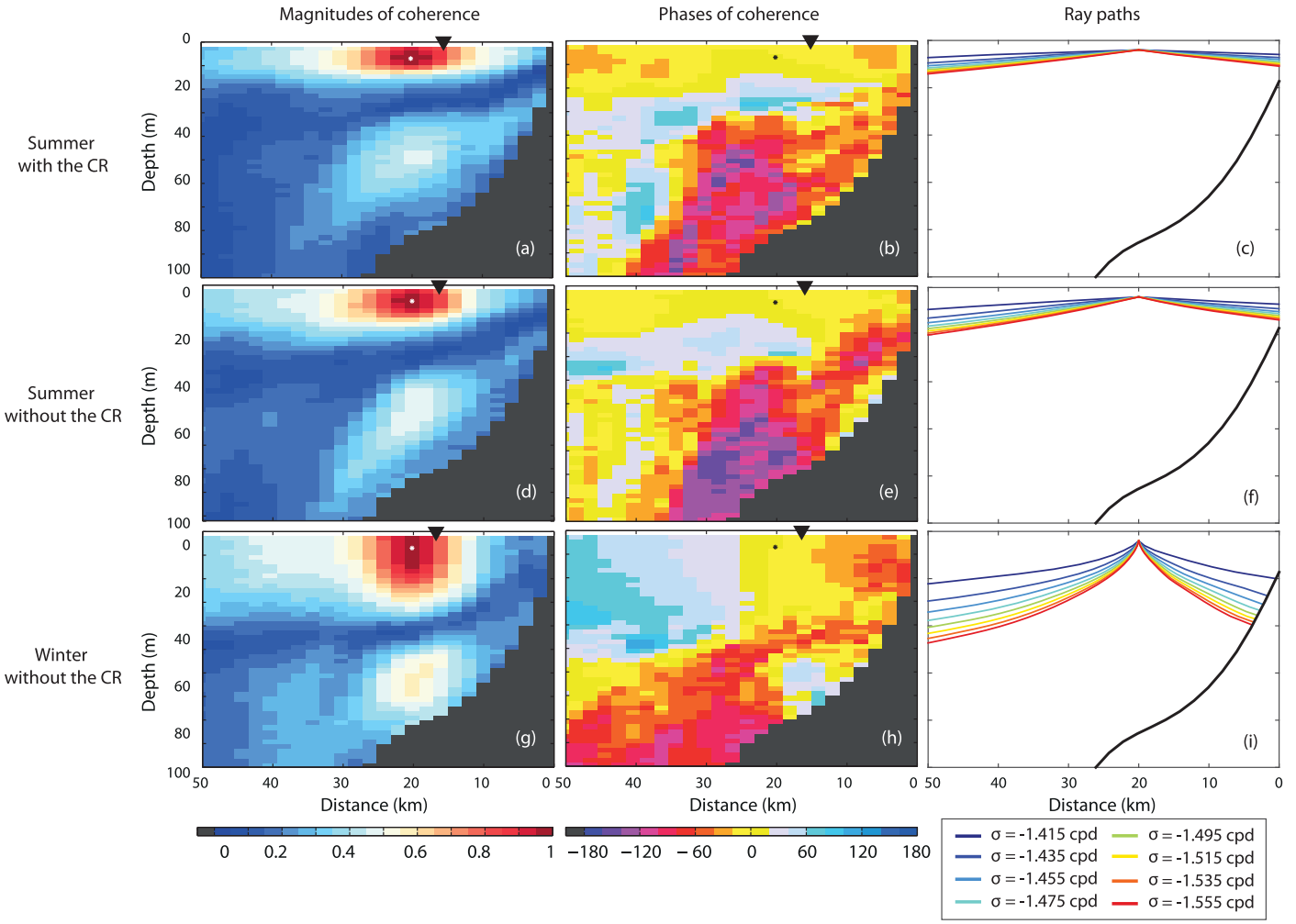

Figure 14. Conditionally estimated coherence of near-inertial subsurface currents referenced at a location of near-surface and nearby NH10 mooring and raypaths estimated from conditionally averaged cross-shore transects of the buoyancy frequency for internal waves at individual frequencies (σ) within the clockwise near-inertial frequency band ($-1.555 \leq \sigma^{-} \leq -1.255$ cpd). (a, d, and g) Magnitudes of coherence. (a) $|\hat{c}^{-}_{\bullet,S}|$, (d) $|\hat{c}^{-}_{\circ,S}|$, and (g) $|\hat{c}^{-}_{\circ,W}|$. (b, e, and h) Phases of coherence. (b) $\theta^{-}_{\bullet,S}$, (e) $\theta^{-}_{\circ,S}$, and (h) $\theta^{-}_{\circ,W}$. (c, f, and i) Raypaths. (c) $l^{-}_{\bullet,S}$, (f) $l^{-}_{\circ,S}$, and (i) $l^{-}_{\circ,W}$. Note that raypaths of internal waves, generated from 160 km offshore and 150 m depth (Figure 15), stop at the continental slope, and the raypaths of internal waves passing by the same reference location (e.g., near-surface and nearby NH10 mooring location) are only presented.

shoreline, the phase propagates upward onshore over the continental shelf, bounces off the coast, then propagates upward offshore, and increases offshore in the upper layer (Figures 13l and 13r), consistent with coastal inhibition [e.g., *Kundu*, 1976; *Millot and Crepon*, 1981; *Pettigrew*, 1981; *Flagg*, 1977]. Although the phase can vary with the reference location, the propagating features and direction are nearly identical (Figures 13j–13m, 13o, and 13q).

The seasonal variation of phases of clockwise near-inertial currents in the cross-shore direction is presented with the coherence referenced at near-surface NH10 mooring location for the three cases ($\hat{c}^{-}_{\bullet,S}$, $\hat{c}^{-}_{\circ,S}$, and $\hat{c}^{-}_{\circ,W}$) (Figure 14). Near surface, the region of the enhanced magnitudes of coherence is nearly as deep as the seasonal mixed layers (Figures 14a, 14d, and 14g). The upward propagations over the continental shelf are persistent over the year (Figure 13r), and the downward offshore phase propagations at surface are better organized during winter than summer (Figures 14b, 14e, and 14h). The enhanced stratification due to riverine water leads to the clockwise near-inertial currents, which are surface-intensified and have horizontally longer length scales in the cross-shore direction (Figures 14a and 14d).

3.3.2. Ray Tracing

The raypaths (l_k, z_k) of internal waves at a frequency of interest (σ) under a given buoyancy frequency are estimated with the piecewise slopes ($\Delta z/\Delta l$) of the ray in the cross-shore transect [e.g., *Jones*, 1969; *Broutman et al.*, 2004]:

$$\frac{\Delta z}{\Delta l} = \frac{z_{k+1} - z_k}{l_{k+1} - l_k} = \pm \sqrt{\frac{\sigma^2 - f_c^2}{\langle N^2_{l_k, z_k} \rangle - \sigma^2}}, \tag{12}$$

where N_{l_k,z_k} indicates the buoyancy frequency at the cross-shore offshore distance (l_k) and the depth (z_k) and can be estimated with bilinear interpolation of the buoyancy frequency data at the nearby vertical bins:

$$N_{l_k,z_k} = \frac{(l_{m+1} - l_k)N_{m,k} + (l_k - l_m)N_{m+1,k}}{l_{m+1} - l_m}, \tag{13}$$

and m and k denotes the cross-shore and vertical depth indices in the numerical model outputs ($m = 1, 2, \cdots, M$ and $k = 1, 2, \cdots, K$). The ray tracing is useful to examine the propagation paths and possible generation locations. In particular, they will show more clearly the superinertial phase propagation pattern near coast, due to coastal inhibition, and seasonal differences.

The raypaths for internal waves generated from 160 km offshore and 150 m depth are computed using an entire year averaged transect and three conditionally averaged transects of the buoyancy frequency (Figures 6d, 6h, and 6l), which can highlight the coastal inhibition showing the reflection at the coastal boundary and the surface (Figure 15). The individual paths correspond to internal waves at individual frequencies within clockwise near-inertial frequency band ($-1.555 \leq \sigma^- \leq -1.255$ cpd). Although the raypaths at each frequency are different (Figure 15a), they mostly show the onshore propagation and the reflection at the continental slope and the surface, consistent with phase propagation patterns (Figure 13r). The reflection at the surface and their offshore propagations depend on the vertical stratification due to seasonal heat fluxes and freshwater inputs (Figures 15b–15d).

To highlight the influence of vertical stratification, the raypaths passing by the same reference location, i.e., near surface and nearby NH10 mooring location, are presented as the magnified views (Figures 14c, 14f, and 14i), which exhibits the vertically asymmetric propagations of the near-inertial internal motions [e.g., *Leaman and Sanford*, 1975]. Onshore propagating subsurface raypaths generated from 160 km offshore and 150 depth (no reflection on the continental slope) are included to present the consistency of the phase propagation (Figures 14b, 14e, and 14h).

4. Summary and Discussion

We investigated the influence of varying horizontal and vertical stratification in the upper layer ($O(10)$ m), which can be caused by coastal riverine waters and seasonal atmospheric fluxes, on coastal near-inertial currents, using in situ observations of surface and subsurface currents and realistic numerical model outputs off the Oregon coast. In this coastal area, vertical stratification is strongly affected by coastal upwelling and downwelling, especially near the coast, freshwater inputs by the CR and seasonal heat fluxes, which implies that the dominant density variation is associated with salinity during summer and temperature during winter. The influence of these two factors is investigated with a transfer function analysis on near-inertial motions, which can isolate the directly wind-coherent currents in a specific frequency band—the clockwise near-inertial frequency band.

Based on ROMS simulations with and without the CR under identical conditions of seasonal heat fluxes, the directly wind-forced near-inertial surface currents are enhanced by up to 60% when the near-surface layer shows a stratified condition due to riverine waters, which corresponds with a low-salinity footprint from the CR. In addition, the simulation without the CR under seasonal stratification indicates that the directly wind-forced near-inertial surface currents during summer are 20%–70% stronger than those during winter, depending on the cross-shore location. This is in contrast to the seasonal patterns of the mixed-layer depth and amplitudes of near-inertial currents.

The coastal inhibition of near-inertial currents in the coastal region is presented with their spatial coherence in the cross-shore direction, in which upward phase propagation over the continental shelf reflects at the coast, then increases upward offshore and downward offshore at the surface, with the magnitudes and length scales in the near-surface layer increasing offshore. This pattern exhibits a particularly well-organized structure during winter. Similarly, the raypaths of clockwise near-inertial internal waves are consistent with the phase propagation of coherence, showing the influence of upper layer stratification and coastal

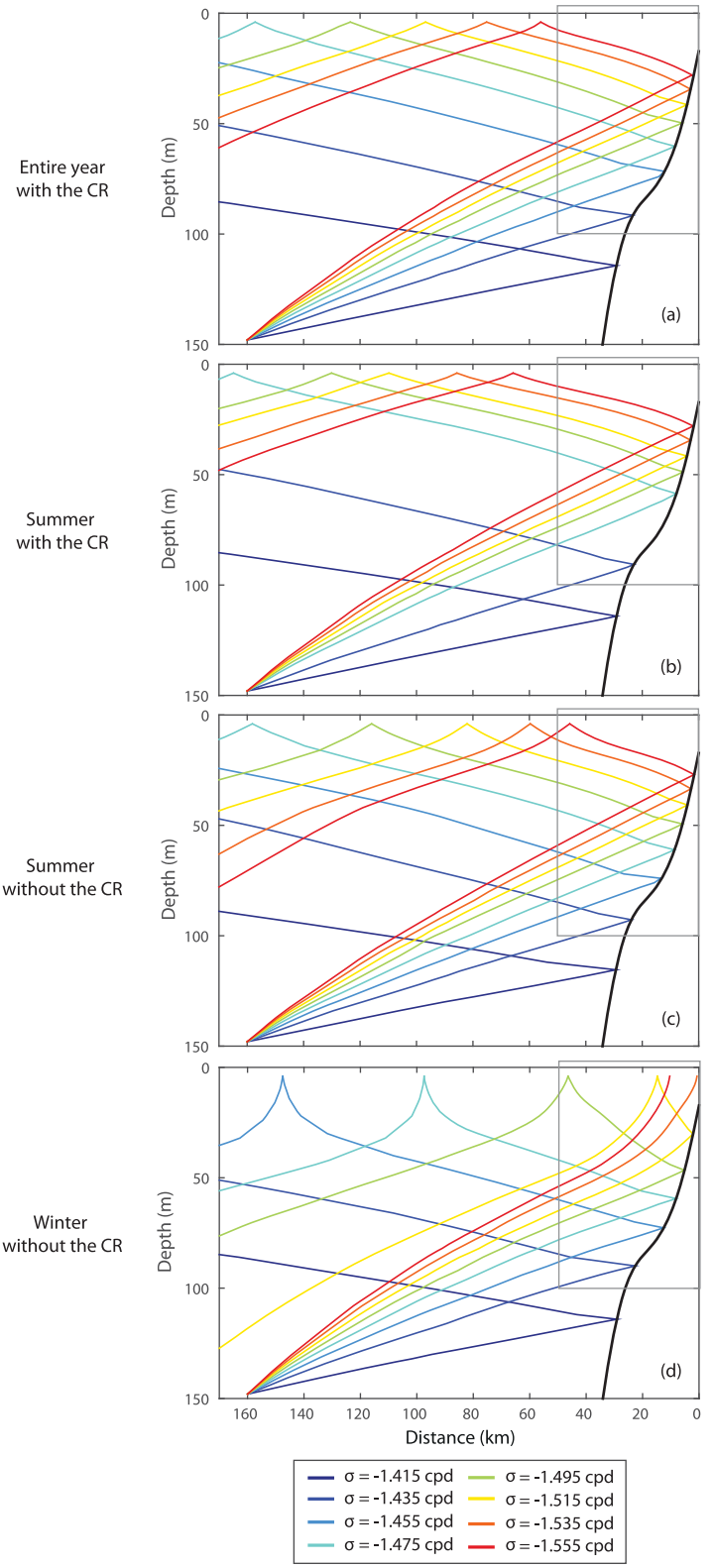

Figure 15. Raypaths for internal waves generated from 160 km offshore and 150 m depth are computed using an entire year averaged cross-shore transect and conditionally averaged cross-shore transects of the buoyancy frequency within the clockwise near-inertial frequency band ($-1.555 \leq \sigma^{-} \leq -1.255$ cpd). (a) $I_{\cdot}^{-}$, (b) $I_{\cdot,S}^{-}$, (c) $I_{\circ,S}^{-}$, and (d) $I_{\cdot,W}^{-}$. Note that gray boxes indicate the nearshore area shown in Figure 14.

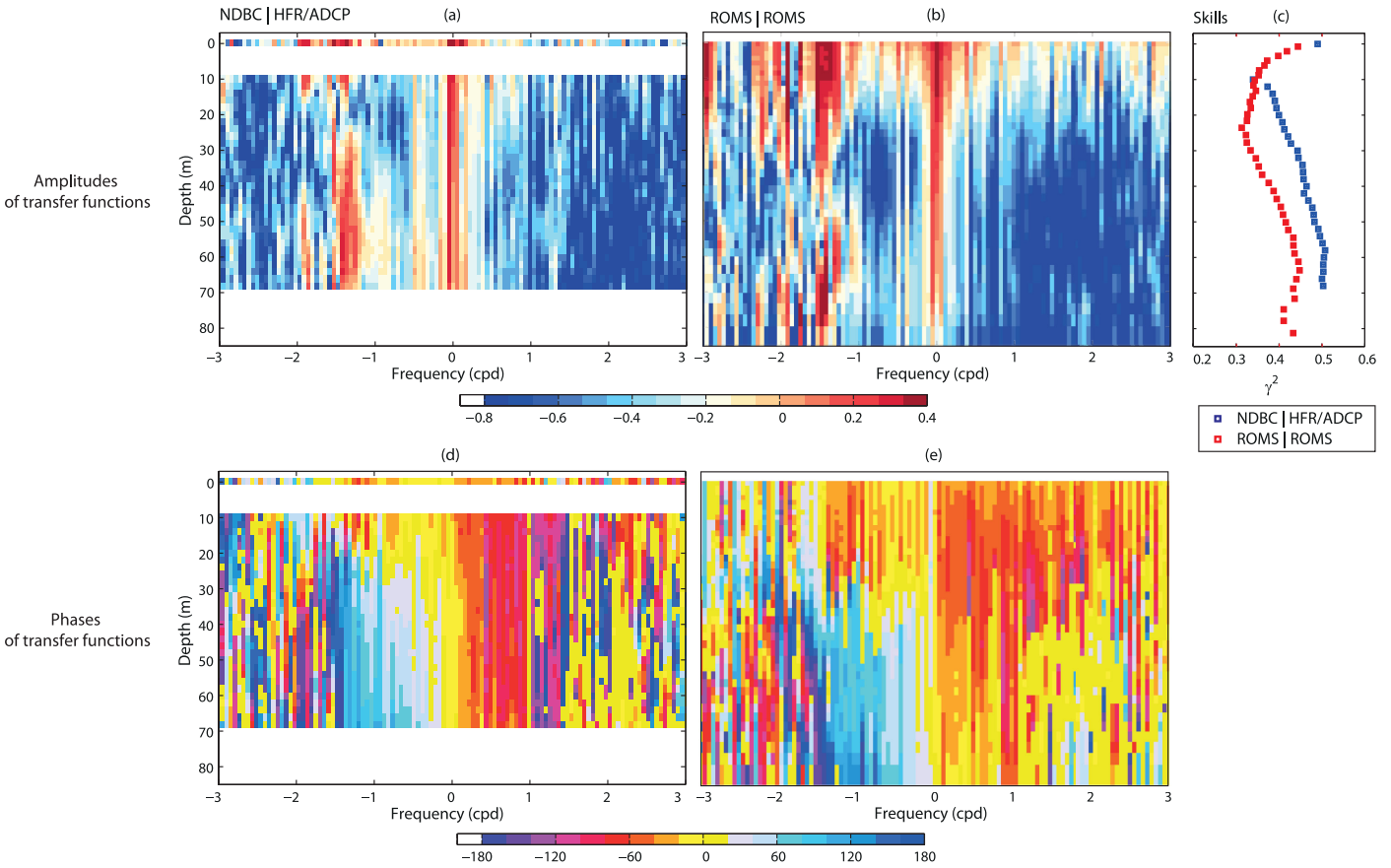

Figure 16. Isotropic transfer functions estimated from (a and c) observations of surface and subsurface currents at the NH10 mooring location and the wind at the Stonewall bank NDBC buoy and (b and d) ROMS simulations with the CR for the entire year. (a and b) Amplitudes of transfer functions ($|\mathbf{H}|$; kg^{-1} m^2 s). (c) Skills. (d and e) Phases of transfer functions (Θ; degrees).

inhibition. The modulation by freshwater inputs and seasonal heat fluxes can lead to energetic mixing and vertical energy propagation by near-inertial motions in the coastal regions.

In the coastal areas, the near-inertial motions are restricted due to coastal boundaries, which implies that their length and time scales decrease onshore and their vertical motions are bounced at the boundaries. In contrast, in the offshore regions, the near-inertial internal waves have more coherent vertical structure. Thus, the aspect ratio in which the ratio of vertical length scale to the horizontal length scale of near-inertial internal waves can be used to characterize their structure. For instance, comparing the aspect ratios above and below the seasonal mixed layer, the one in the upper layer is higher than the other one as a result of the enhanced vertical length scale in the lower layer.

Appendix A: Wind Transfer Function at the Mooring

The isotropic wind transfer functions with depth, estimated from the observed wind stress and surface/subsurface currents and the ROMS wind stress and currents over the entire records for a period of approximately 1 year, are shown in Figure 16. The enhanced amplitudes of transfer functions in the clockwise near-inertial frequency band appear from the surface to the upper 20 m for ADCP and 40 m for ROMS and decrease with depth because the degree of penetration of the wind stress momentum decreases (Figures 16a and 16b). At low frequency ($|\sigma| \leq 0.2$ cpd), the transfer functions become significant at most of the depths because the wind-driven geostrophic balance is dominant at that mooring location [e.g., *Kim et al.*, 2009a]. The phases of the transfer functions are consistent with the analytical models (Figures 16c and 16d) [e.g., *Kim and Kosro*, 2013; *Kim et al.*, 2015].

Acknowledgments
Sung Yong Kim is supported by the Basic Science Research Program through the National Research Foundation (NRF), Ministry of Education (NRF-2013R1A1A2057849), and the Human Resources Development of the Korea Institute of Energy Technology Evaluation and Planning (KETEP), Ministry of Trade, Industry and Energy (no. 20114030200040), Republic of Korea. Alexander L. Kurapov is supported by the National Science Foundation (NSF) (grants OCE-0434810, OCE-0648314, and OCE-1030922), the Office of Naval Research Physical Oceanography Program (grant N000140810942) (including CIOSS and IOOS-NANOOS). P. Michael Kosro is supported by the NSF (grants 0000734, 0434810, and 0237710) and the NOAA IOOS program (most recently NA11NOS0120036). Surface current and wind data are provided by Oregon State University and National Data Buoy Center (NDBC), respectively. M. D. Levine made the moored measurements of temperature and salinity at NH10 described in section 2.3.2, with NANOOS funding. The data used in the paper will be available from the authors upon request (syongkim@kaist.ac.kr) to comply with the American Geophysical Union Publications Data Policy.

References

Alford, M. H., and M. C. Gregg (2001), Near-inertial mixing: Modulation of shear, strain and microstructure at low latitude, *J. Geophys. Res.*, *106*(C8), 16,947–16,968, doi:10.1029/2000JC000370.

Arakawa, A. (1966), Computational design for long-term numerical integration of the equations of fluid motion: Two-dimensional incompressible flow. Part I, *J. Comput. Phys.*, *1*(1), 119–143.

Banas, N., P. MacCready, and B. Hickey (2009), The Columbia River plume as cross-shelf exporter and along-coast barrier, *Cont. Shelf Res.*, *29*(1), 292–301.

Berdeal, I. G., B. M. Hickey, and M. Kawase (2002), Influence of wind stress and ambient flow on a high discharge river plume, *J. Geophys. Res.*, *107*(C9), 3130, doi:10.1029/2001JC000932.

Broutman, D., J. W. Rottman, and S. D. Eckermann (2004), Ray methods for internal waves in the atmosphere and ocean, *Annu. Rev. Fluid Mech.*, *36*, 233–253.

Choi, B.-J., and J. L. Wilkin (2007), The effect of wind on the dispersal of Hudson river plume, *J. Phys. Oceanogr.*, *37*(7), 1878–1897, doi:10.1175/JPO3081.1.

Crawford, G. B., and W. G. Large (1996), A numerical investigation of resonant inertial response of the ocean to wind forcing, *J. Phys. Oceanogr.*, *26*(6), 873–891.

Crepon, M. (1969), Hydrodynamique marine en regime impulsionnel, *Cah. Oceanogr.*, *21*, 863–877.

D'Asaro, E., and H. Perkins (1984), A near-inertial internal wave spectrum for the Sargasso Sea in late summer, *J. Phys. Oceanogr.*, *14*(3), 489–505.

D'Asaro, E. A. (1985), The energy flux from the wind to the near-inertial motions in the surface mixed layer, *J. Phys. Oceanogr.*, *15*(8), 1043–1059.

Emery, W. J., and R. E. Thomson (1997), *Data Analysis Methods in Physical Oceanography*, 634 pp., Elsevier, Boston, Mass.

Flagg, C. N. (1977), The dynamics and kinematics of the New England continental shelf and shelf/slope front, PhD thesis, Mass. Inst. of Technol., Dep. of Meteorol., Cambridge. [Available at http://hdl.handle.net/1721.1/52836.]

Gan, J., L. Li, D. Wang, and X. Guo (2009), Interaction of a river plume with coastal upwelling in the northeastern South China Sea, *Cont. Shelf Res.*, *29*(4), 728–740, doi:10.1016/j.csr.2008.12.002.

Gregg, M., and M. G. Briscoe (1979), Internal waves, finestructure, microstructure, and mixing in the ocean, *Rev. Geophys.*, *17*(7), 1524–1548.

Hickey, B., S. Geier, N. Kachel, and A. MacFadyen (2005), A bi-directional river plume: The Columbia in summer, *Cont. Shelf Res.*, *25*(14), 1631–1656, doi:10.1016/j.csr.2005.04.010.

Hickey, B. M., et al. (2010), River influences on shelf ecosystems: Introduction and synthesis, *J. Geophys. Res.*, *115*, C00B17, doi:10.1029/2009JC005452.

Jones, W. L. (1969), Ray tracing for internal gravity waves, *J. Geophys. Res.*, *74*(8), 2028–2033, doi:10.1029/JB074i008p02028.

Kim, S. Y. (2014), A statistical description on the wind-coherent responses of sea surface heights off the U.S. West Coast, *Ocean Dyn.*, *64*(1), 29–46, doi:10.1007/s10236-013-0668-3.

Kim, S. Y., and P. M. Kosro (2013), Observations of near-inertial surface currents off Oregon: Decorrelation time and length scales, *J. Geophys. Res.*, *118*, 3723–3736, doi:10.1002/jgrc.20235.

Kim, S. Y., B. D. Cornuelle, and E. J. Terrill (2009a), Anisotropic response of surface currents to the wind in a coastal region, *J. Phys. Oceanogr.*, *39*(6), 1512–1533, doi:10.1175/2009JPO4013.1.

Kim, S. Y., E. J. Terrill, and B. D. Cornuelle (2009b), Assessing coastal plumes in a region of multiple discharges: The U.S.–Mexico border, *Environ. Sci. Technol.*, *43*(19), 7450–7457, doi:10.1021/es900775p.

Kim, S. Y., et al. (2011), Mapping the U.S. West Coast surface circulation: A multiyear analysis of high-frequency radar observations, *J. Geophys. Res.*, *116*, C03011, doi:10.1029/2010JC006669.

Kim, S. Y., P. M. Kosro, and A. L. Kurapov (2014), Evaluation of directly wind-coherent near-inertial surface currents off Oregon using a statistical parameterization and analytical and numerical models, *J. Geophys. Res.*, *119*, 6631–6654, doi:10.1002/2014JC010115.

Kim, S. Y., G. Gopalakrishnan, and A. Ponte (2015), Interpretation of coastal wind transfer functions with momentum balances derived from idealized numerical model simulations, *Ocean Dyn.*, *65*(1), 115–141, doi:10.1007/s10236-014-0766-x.

Kosro, P. M. (2003), Enhanced southward flow over the Oregon shelf in 2002: A conduit for subarctic water, *Geophys. Res. Lett.*, *30*(15), 8023, doi:10.1029/2003GL017436.

Kosro, P. M. (2005), On the spatial structure of coastal circulation off Newport, Oregon, during spring and summer 2001 in a region of varying shelf width, *J. Geophys. Res.*, *110*, C10S06, doi:10.1029/2004JC002769.

Kourafalou, V. H., L.-Y. Oey, J. D. Wang, and T. N. Lee (1996), The fate of river discharge on the continental shelf: 1. Modeling the river plume and the inner shelf coastal current, *J. Geophys. Res.*, *101*(C2), 3415–3434, doi:10.1029/95JC03024.

Krauss, W. (1972), Wind-generated internal waves and inertial-period motions, *Dtsch. Hydrogr. Z.*, *25*(6), 241–250.

Krauss, W. (1979), Inertial waves in an infinite channel of rectangular cross section, *Dtsch. Hydrogr. Z.*, *32*, 248–266.

Kundu, P. K. (1976), An analysis of inertial oscillations observed near Oregon coast, *J. Phys. Oceanogr.*, *6*, 879–893.

Kundu, P. K. (1984), Generation of coastal inertial oscillations by time-varying wind, *J. Phys. Oceanogr.*, *14*(12), 1901–1913.

Kundu, P. K., S.-Y. Chao, and J. P. McCreary (1983), Transient coastal currents and inertio-gravity waves, *Deep Sea Res., Part A*, *30*(10), 1059–1082, doi:10.1016/0198-0149(83)90061-4.

Kurapov, A. L., G. D. Egbert, J. S. Allen, R. N. Miller, S. Y. Erofeeva, and P. M. Kosro (2003), The M_2 internal tide off Oregon: Inference from data assimilation, *J. Phys. Oceanogr.*, *33*, 1733–1757.

Large, W., J. McWilliams, and S. Doney (1994), Oceanic vertical mixing: A review and a model with a non-local boundary layer parameterization, *Rev. Geophys.*, *32*(4), 363–403, doi:10.1029/94RG01872.

Leaman, K. D., and T. B. Sanford (1975), Vertical energy propagation of inertial waves: A vector spectral analysis of velocity profiles, *J. Geophys. Res.*, *80*(15), 1975–1978.

Millot, C., and M. Crepon (1981), Inertial oscillations on the continental shelf of the Gulf of Lions: Observations and theory, *J. Phys. Oceanogr.*, *11*, 639–657.

O'Donnell, J. (1990), The formation and fate of a river plume: A numerical model, *J. Phys. Oceanogr.*, *20*, 551–569.

Osborne, J., A. Kurapov, G. Egbert, and P. Kosro (2011), Spatial and temporal variability of the M_2 internal tide generation and propagation on the Oregon shelf, *J. Phys. Oceanogr.*, *41*(11), 2037–2062.

Osborne, J. J., A. L. Kurapov, G. D. Egbert, and P. M. Kosro (2014), Intensified diurnal tides along the Oregon Coast, *J. Phys. Oceanogr.*, 7(*44*), 1689–1703, doi:10.1175/JPO-D-13-0247.1.

Pettigrew, N. R. (1981), The dynamics and kinematics of the coastal boundary layer off Long Island, PhD thesis, Mass. Inst. of Technol., Dep. of Meteorol. and Phys. Oceanogr., Cambridge. [Available at http://hdl.handle.net/1721.1/27913.]

Pollard, R. T., and R. C. Millard (1970), Comparison between observed and simulated wind-generated inertial oscillations, *Deep Sea Res. Oceanogr. Abstr.*, *17*, 813–821, doi:10.1016/0011-7471(70)90043-4.

Price, J. F., R. A. Weller, and R. Pinkel (1986), Diurnal cycling: Observations and models of the upper ocean response to diurnal heating, cooling, and wind mixing, *J. Geophys. Res.*, *91*(C7), 8411–8427, doi:10.1029/JC091iC07p08411.

Rainville, L., and R. A. Woodgate (2009), Observations of internal wave generation in the seasonally ice-free arctic, *Geophys. Res. Lett.*, *36*, L23604, doi:10.1029/2009GL041291.

Shearman, R. K. (2005), Observations of near-inertial current variability on the New England shelf, *J. Geophys. Res.*, *110*, C02012, doi: 10.1029/2004JC002341.

Shrira, V. I., and P. Forget (2015), On the nature of near-inertial oscillations in the uppermost part of the ocean and a possible route toward HF radar probing of stratification, *J. Phys. Oceanogr.*, *45*, 2660–2678, doi:10.1175/JPO-D-14-0247.1.

Verspecht, F., J. Simpson, and T. Rippeth (2010), Semi-diurnal tidal ellipse variability in a region of freshwater influence, *Geophys. Res. Lett.*, *37*, L18602, doi:10.1029/2010GL044470.

Warrick, J., P. M. DiGiacomo, S. B. Weisberg, N. P. Nezlin, M. Mengel, B. H. Jones, J. C. Ohlmann, L. Washburn, E. J. Terrill, and K. L. Farnsworth (2007), River plume patterns and dynamics within the Southern California Bight, *Cont. Shelf Res.*, *27*(19), 2427–2448, doi: 10.1016/j.csr.2007.06.015.

Zervakis, V., and M. Levine (1995), Near-inertial energy propagation from the mixed layer: Theoretical considerations, *J. Phys. Oceanogr.*, *25*(11), 2872–2889.